UNIVERSITY OF OKLAHOMA

GRADUATE COLLEGE

ADVANCING MULTIMODAL APPROACHES TO STUDY HUMAN BRAIN: IMPROVEMENTS IN SIMULTANEOUS EEG-FMRI ACQUISITION

A DISSERTATION

SUBMITTED TO THE GRADUATE FACULTY

in partial fulfillment of the requirements for the

Degree of

DOCTOR OF PHILOSOPHY

IN

ELECTRICAL AND COMPUTER ENGINEERING

By

AHMAD MAYELI
Norman, Oklahoma
2019

ADVANCING MULTIMODAL APPROACHES TO STUDY HUMAN BRAIN:

IMPROVEMENTS IN SIMULTANEOUS EEG-FMRI ACQUISITION

A DISSERTATION APPROVED FOR THE
SCHOOL OF ELECTRICAL AND COMPUTER ENGINEERING

BY

_____
Dr. Hazem Refai, Chair

_____
Dr. Jerzy Bodurka, Co-Chair

_____
Dr. James Sluss

_____
Dr. Thordur Runolfsson

_____
Dr. Vickie Lake

Acknowledgments

First and foremost, I am deeply grateful to my advisors, Dr. Jerzy Bodurka and Dr. Hazem Refai, for their consistent support and providing me with guidance and encouragement. Dr. Jerzy Bodurka has provided me incredible support to find my research way and giving me an invaluable research opportunity to work on this project. Dr. Hazem Refai helped me with unconditional advice, support, and generosity through my Ph.D. I am very grateful to my Ph.D. committee members Dr. Thordur Runolfsson, Dr. James Sluss, and Dr. Vickie Lake for their comments, feedback, and guidance.

At the Laureate Institute for Brain Research, my sincerest appreciation goes to Dr. Vadim Zotev, Dr. Masaya Misaki, Dr. Qingfei Luo, and Dr. Aki Tsuchiyagaito for all their support and invaluable advice. It could not be possible for me to finish this work without their help and support. In addition, I would like to thanks all other Dr. Bodurka's lab members, principle investigators, and staffs at Laureate Institute for Brain Research, especially Dr. Hamed Ekhtiari, Dr. Evan White, Dr. Sahib Khalsa and Dr. Jennifer Stewart for their support, friendship and contributions to my research during my graduate study.

I gratefully acknowledge the financial support from the Laureate Institute for Brain Research and the agencies that funded my work: William K. Warren Foundation, National Institute of General Medical Sciences, National Institutes of Health.

I would like to give special thanks to my great friends, Dr. Masoud Allahkarami, Dr. Leila Seyed Faraji, and Dr. Obada Al Zoubi, for always encouraging me and being supportive.

Finally, I would like to express my deepest appreciation and dedicate this work to my beloved parents, Keykavous Mayeli and Esmat Soleimani and my sisters, Mina, Leili and Zibandeh Mayeli for their willing encouragement and support during my study over the years.

Table of Contents

Acknowledgments ..... **iv**

List of Tables ..... **viii**

List of Figures ..... **ix**

Abstract ..... **xii**

Chapter 1: Introduction **1**

1.1 Thesis Overview 2

Chapter 2: Neuroimaging Modalities **4**

2.1 Introduction 4

2.2 EEG 5

2.3 fMRI 7

2.4 Simultaneous EEG-fMRI 8

2.5 Pupilometry 12

Chapter 3: Automated Pipeline for EEG Artifact Reduction Recorded during fMRI (APPEAR) **13**

3.1 Introduction 13

3.2 Methods 15

3.2.1 APPEAR 15

3.2.1.1 AAS/OBS and Filtering 16

3.2.1.2 ICA 19

3.2.1.3 Automatic IC Classification 20

3.2.1.4 Reconstructing EEG Data after ICA Decomposition 30
3.2.2 Data Acquisition 30
3.2.3 Evaluation 31
3.2.3.1 Stop Signal ERP 32
3.2.3.2 Resting-State 34
3.3 Results 35
3.4 Conclusion 46
Chapter 4: Integration of Simultaneous Resting-State EEG, fMRI, and Eye Tracker Methods to Determine and Verify Vigilance Metrics 49
4.1 Introduction 49
4.2 Data Collection 52
4.3 Data Analysis 53
4.3.1 Preprocessing 54
4.3.2 Postprocessing 56
4.4 Results 58
4.5 Discussion 69
4.6 Conclusion 73
Chapter 5: Conclusion and Future Work 75
5.1 Conclusion 75
5.2 Future Works 76
References 78
Appendix A. Abbreviations 88

List of Tables

Table 2-1. EEG frequency bands 6

Table 3-1. *T*-tests comparing mean amplitude N2, P3 across automated and manual processing. 36

Table 3-2. *T*-tests comparing signal-to-noise ratios N2 and P3 across automated and manual processing. 38

Table 3-3. Signal-to-noise ratios by individual subjects for the N2 Automated 39

Table 3-4. Signal-to-noise ratios by individual subjects for the P3 Automated 39

Table 3-5. Signal to noise ratios in the grand average waveforms. 40

Table 3-6. Signal-to-noise ratios by individual subjects for the N2 Manual in the grand average waveforms 41

Table 3-7. Signal-to-noise ratios by individual subjects for the P3 Manual in the grand average waveforms. 41

Table 4-1. Percentages of missing pupil size data 55

Table 4-2. The details of correlations between pupil size and EEG features. 58

Table 4-3. Brain regions correlated to power spectral density in frontal and occipital beta power (FOBP). 62

Table 4-4. Brain regions correlated to power spectral density in the beta band (channels F3, F4, Fz, O1, O2, and Oz) without physiological noise correction. 63

Table 4-5. Brain regions correlated to pupil size. 67

Table 4-6. Brain regions correlated to pupil size without physiological noise correction. 69

List of Figures

Figure 2-1: EEG time course with gradient artifact (sampled at 5000 S/s) and after reducing that artifact with average artifact subtraction (AAS) sampled at 250 S/s. 10

Figure 2-2: EEG time course with ballistocardiogram (BCG) artifact and its reduced artifact using average artifact subtraction (AAS) both sampled at 250 S/s..... 11

Figure 3-1: The APPEAR Flowchart. 18

Figure 3-2: Comparison between Power Spectral Density (PSD) After Applying Average Artifact Subtraction (AAS, black line) and Optimal Basis Sets (OBS, red line). 19

Figure 3-3: An Example of Ballistocardiogram (BCG) Component..... 25

Figure 3-4: An Example of Blink Component. Blink ICs can be identified by their strong spatial projection in the frontal area and low frequency activity in delta band..... 26

Figure 3-5: An Example of a Single Channel Component. This type of artifact affects mostly one or two electrodes due to either strong muscle activity around that electrode or to poor contact. 28

Figure 3-6: An Example of Muscle Component. Muscle electrical activity or "electromyogenic" (EMG) artifacts exhibit widespread high-frequency activity due to asynchronous motor action units. These components are flagged if the power of the signal is spread out in frequencies higher than 30 Hz, known as the gamma band. 29

Figure 3-7: Comparison of waveforms (A) and topographical maps for ERP waveforms after applying APPEAR and manual correction (B1: N2 scalp topography from the

automated correction; C1: N2 scalp topography from the manual correction; B2: P3 scalp topography from the automated correction; C2: P3 scalp topography from the manual correction)..... 37

Figure 3-8: The time/frequency comparison (Wavelet) between APPEAR (upper rows) and manually-corrected EEG data (lower rows) for all individual subjects. 45

Figure 3-9: Powers Spectral Density (PSD) Comparison between AAS, APPEAR, and Manually Corrected EEG Data in (A) Delta; (B) Theta; (C) Alpha; and (D) Beta band. 46

Figure 4-1: The data analysis flowchart. 54

Figure 4-2: Association between following EEG features from frontal (i.e., (F3, F4, and Fz) and occipital (O1, O2, and Oz)) electrodes: (A) Alpha power; (B) Beta power; (C) Alpha ration and the pupil size. 59

Figure 4-3: Association between the following average EEG features among all channels: (A) Alpha power; (B) Beta power; (C) Alpha ration, and pupil size. 60

Figure 4-4: Power spectral density in the frontal and occipital beta power (FOBP) correlation Map. 62

Figure 4-5: Power spectral density in the frontal and occipital beta power (FOBP) correlation Map without physiological noise correction. 63

Figure 4-6: Association between frontal and occipital beta power (FOBP) and heart rate. 65

Figure 4-7: Association Between EEG Power in Beta Band and heart rate..... 65

Figure 4-8: Pupil size correlation map achieved by using pupil size as a regressor in fMRI GLM analysis. 66

Figure 4-9: Pupil size correlation map without physiological noise correction, achieved by using pupil size as a regressor in fMRI GLM analysis. 68

Abstract

The primary aim of the study detailed in this dissertation was improving the quality of simultaneous electroencephalography (EEG) and functional magnetic resonance imaging (fMRI) experiments. Two common challenges to use concurrent EEG-fMRI tests are addressed herein. The first is the presence of EEG artifacts during simultaneous EEG-fMRI, which require more consideration than EEG data recorded outside the scanner. To mitigate this issue, a fully automated artifact correction pipeline was developed. In the proposed pipeline, magnetic resonance (MR) environmental (i.e., gradient and ballistocardiogram [BCG]) artifacts were reduced using optimal basis sets (OBS) and average artifact subtraction (AAS). Subsequently, independent component analysis (ICA) was leveraged for reducing physiological artifacts (e.g., eye blinks, saccade and muscle artifacts), in addition to residual BCG artifacts. To validate pipeline performance, both resting-state (time/frequency and frequency analysis) and task-based (event related potential [ERP]) EEG data from eight healthy participants were tested. This data was compared with the time/frequency and frequency results achieved by matching meticulously, manually corrected EEG data to the automatically corrected EEG data. No significant difference was found between results. A comparison between ERP results (e.g., amplitude measures and SNR) also showed no differences between manually corrected and fully automated EEG corrected data. The second challenge addressed in this work is the low experimental control over the subject's actual behavior during the eyes-open resting-state fMRI (rsfMRI). This technique has been widely used for studying the (presumably) awake and alert human brain using multimodal EEG-fMRI; however,

objective and verified experimental measures to quantify the degree of alertness (e.g., vigilance) are not readily available. To this end, the study reported in this dissertation investigated whether simultaneous multimodal EEG, rsfMRI and eye-tracker experiments could be used to extract objective and robust biomarkers of vigilance in healthy human subjects (n = 10) during cross fixation. Frontal and occipital beta power (FOBP) were found to correlate ($r = 0.306$, $p<0.001$) with pupil size fluctuation, which is an indirect index for locus coeruleus activity implicated in vigilance regulation. Moreover, FOBP was also correlated with heart rate ($r = 0.255$, $p<0.001$) and several brain regions in an anti-correlated network, including the bilateral insula and inferior parietal lobule. Results support the conclusion that FOBP is an objective and robust biomarker of vigilance in healthy human subjects.

Chapter 1: Introduction

The brain is the most critical and complex organ in the human body. Not only does the brain control cognitive functions (e.g., emotion, memory, and sense), but more importantly, it controls vital body functions (e.g., breathing, movement, and cardiac functions). Brain research involves varied professionals from many scientific disciplines, spanning from math and physics, engineering, neuroscience, physiology, and more clinically oriented fields such as psychiatry and neurology. Several brain imaging techniques are designed to study brain activity noninvasively and to further diagnose problems and diseases associated with abnormalities in brain functioning and its structures.

This dissertation contributes to the field of multimodal brain neuroimaging in the following ways.

1- The study addressed the quality of EEG data recorded simultaneously with fMRI, which is an ongoing challenge for such experiments. To do so,
   a. the efficiency of removing BCG artifact using two of the most common approaches (i.e., AAS, and OBS) was investigated;
   b. a fully automated pipeline was developed to remove artifacts from EEG acquired with fMRI; and
   c. the automated algorithm was validated with resting-state and task-based EEG data for large scale EEG-fMRI studies.

2- An eye-tracking technique was integrated as a reliable measure of subject attentiveness to find EEG features associated with vigilance for further use in simultaneous EEG-fMRI experiments and to have better control over common paradigm simultaneous EEG-fMRI (i.e., eyes-open resting state). Results showed that

   a. EEG frontal and occipital beta power (FOBP) is associated with pupil size in resting-state fMRI (i.e., eyes-open);
   b. FOBP is positively correlated with heart rate, as well as regions of the anti-correlated network; and
   c. FOBP or heart rate could be proposed as a vigilance-level index in eyes-open rsfMRI.

1.1 Thesis Overview

The remainder of this dissertation is organized in the following way:

Chapter 2: Details of three techniques used in this work are discussed: EEG, fMRI, and pupilometry. Simultaneous EEG-fMRI was the primary modality utilized in this dissertation. Three facets are detailed: 1) the technology and operation of EEG and fMRI, 2) the reason for combining these modalities, and 3) the challenges encountered for such a combination. An overview of the third technique (i.e., pupilometry) used in this work is discussed at the end of this chapter.

Chapter 3: Details the presence of EEG artifacts during simultaneously recording EEG and fMRI. To address this issue, a fully automated pipeline was developed using OBS, AAS, and ICA to reduce all types of artifacts appearing on the EEG signal during fMRI acquisition. The efficiency of the developed pipeline was evaluated using several methods.

Chapter 4: Results from simultaneous eyes-open rsfMRI, EEG, eye-tracking, and heart rate signals recorded from healthy participants were reported. The rsfMRI has recently become an important tool for studying the human brain due to its simplicity and non-invasiveness, as well as its requisite of least effort from subjects. However, an individual's degree of change in vigilance during rsfMRI may affect resting-state network and functional connectivity results. To address this problem from experimental data collected, first, EEG features associated with pupil dimension were determined, and these features were validated by correlating them with heart rate changes associated with arousal. Next, the relationship between these validated EEG features and BOLD fMRI signals was investigated to illustrate the spatial and temporal characteristics of the brain's vigilance response.

Chapter 5: Summarizes the findings of the work reported herein and forecasts future works.

Chapter 2: Neuroimaging Modalities

2.1 Introduction

A number of accepted techniques for imaging and studying brain function have been developed in the last several decades such as functional magnetic resonance imaging (fMRI), positron emission tomography (PET), electroencephalography (EEG), magnetoencephalography (MEG), and functional near infrared spectroscopy (fNIRS) [1]; each is specified by different spatiotemporal resolutions and divided into two categories: direct (e.g., MEG and EEG) and indirect (e.g., PET, NIRS, and fMRI) measurements of neural activities. fMRI is an indirect tool for measuring brain activity that uses ^{1}H nuclear magnetic resonance phenomena and MRI imaging technology. fMRI signal is sensitive to the hemodynamic changes (e.g., blood-oxygenation level dependent [BOLD] contrast) resulted from neuronal activity in brain regions associated with resting-state, response to a task, or cognitive functions such as emotion processing. In order to accommodate increased demand for local neuronal activity, both oxygen consumption and blood flow increase in local brain regions and could be detected and measured with BOLD fMRI. PET utilizes annihilation phenomena of positrons emitted from injected radioactive substances to map functional processes in the brain on a cellular level. Localized increased consumption of radioactive substance and increased count of gamma

rays emitted during positrons and electron annihilations events reflects an increase in brain metabolic activity and is capture and imaged by a PET scanner. Brain electrical activity (e.g., ionic currents resulting from brain neuronal activity) generates electric and magnetic fields both propagate through space and time, and their effects can be measured using electrodes placed on the scalp (EEG) or magnetic field intensity sensors (MEG) surrounding at close proximity of the scalp. Both MEG and EEG measured activities are the summation of synchronous in time and space activity from thousands, sometimes millions, of neurons in the brain [2-5]. MEG often comprises an EEG recording system in order to record EEG-MEG simultaneously. fNIRS is another powerful imaging tool for measuring hemodynamic responses associated with neuron behavior. The changes in blood flow and oxygenation in the brain cortical areas are reflected in absorption spectra of near-infrared light region. Because of limited capacity of near-infrared light to penetrate the whole brain, this technique reflects only brain neuronal activity in cortical areas.

2.2 EEG

Caton first discovered electrical activity in the brain in 1874 [2]. Hans Berger, widely recognized as the father of EEG, published the first EEG results from the human scalp, recorded in 1929 [3]. However, it took an extended period of time for EEG to become an acceptable neuroimaging technique for measuring brain activity, and that didn't happen until EEG alpha rhythm was demonstrated by Adrian and Mattew [4] in human occipital lobes.

EEG represents patterns of both normal and abnormal neural (electrical) activity while individuals are awake and during sleep. Fourier transformation is commonly used to divide EEG signal into certain EEG frequency bands (i.e., delta, theta, alpha, beta, and gamma), shown in Table 2.1. Each of these frequency bands is associated with certain mental properties [5-8]. Delta and theta are low-frequency EEG patterns that appear mostly during sleep. However, low amplitude theta rhythms are also apparent in waking EEG measurements. In general, the alpha rhythm is the predominant EEG wave pattern in an adult in a state of resting wakefulness. Beta rhythms occur when subjects are alert as well as when they are attentive to external stimuli.

Table 2-1. EEG frequency bands

Rhythm	Frequency [Hz]
Delta	0.1-4
Theta	4-7
Alpha	7-13
Beta	13-30
Gamma	>30

One of the main advantages of EEG is its high temporal resolution on the order of milliseconds. However, a drawback for EEG is its poor source spatial localization accuracy, due to individual geometry and conductivity as well as a limited number of EEG electrodes [9].

Further, EEG is a highly sensitive measure that can easily be obscured by unwanted non-cerebral electrical activity (i.e., artifacts)[10]. Eye (ocular), muscle, and movement are common types of EEG artifacts, and each of them affects specific EEG frequency bands. Ocular artifacts can be generated by the subject's eye blinks and eye

movements and primarily appear in the delta range [11]. Myogenic activity due to the contraction of head muscles is the source of muscle artifacts, which are primarily evident in the beta and gamma bands [12]. Head and body or electrode-wire movement can also generate movement artifacts that affect various frequency bands but occur primarily in the delta band [13]. In addition to the aforementioned artifacts, magnetic resonance (MR) environmental artifacts could obscure EEG data further when EEG measurements are recorded inside an MRI scanner. This phenomenon is discussed in greater detail in the next section and next chapter.

2.3 fMRI

Magnetic Resonance Imaging (MRI) is a safe and non-invasive tool for imaging the brain and biological human and animal structures. An MRI machine is composed of a magnet, magnetic gradient coils, a radio frequency (RF) receiver and transmitter, an MRI signal receiver, and a computer for controlling hardware, signal acquisition, and displaying/storing/managing reconstructed MR images [14].

MRI machines are widely used to investigate brain functionality over time, which is known as functional magnetic resonance imaging (fMRI). fMRI relies on the association between neural activities inside the brain and vasculature. Blood-oxygen-level dependent (BOLD) contrast imaging is the most dominant method employed in fMRI. The neural activity uses up oxygen, and the vasculature responds by providing more highly oxygenated blood to local brain regions [15]. This results in a measurable change in the amount of oxygen in the blood, which is taken as the amount of local neural

activity, and the measured signal is known as the BOLD signal. Unlike EEG, fMRI suffers from limited time resolution resulting from slow hemodynamic response. However, it is characterized by high spatial resolution.

2.4 Simultaneous EEG-fMRI

Each neuroimaging modality has its own advantages and disadvantages. In studying the complexities of the human brain, combining modalities helps integrate different advantages from varying modalities and leverages their disadvantages to better understand brain structure and functionality. EEG and fMRI are the most widespread, noninvasive, and safest techniques for detecting and characterizing relevant changes in brain states and further investigating their relationships with neuronal activity. Notably, combining neuroimaging techniques is not limited to EEG-fMRI. However, combining these two modalities (i.e., EEG and fMRI) is beneficial since they can compensate for each other's weaknesses very well. In other words, simultaneous EEG-fMRI leverages the high temporal resolution of the EEG and the high spatial resolution of the fMRI. Furthermore, EEG is a direct measure of brain activity, and fMRI is an indirect measure; therefore, simultaneous EEG-fMRI measurements can aid in cross-validation. Despite the advantages of combining EEG and fMRI, three main challenges must be considered when simultaneously acquiring these two modalities: patient safety, EEG quality, and fMRI image quality [16]. Two considerations must be taken into account regarding simultaneous EEG-fMRI safety. The first is that the ferromagnetic materials should not be taken into the scanner. The second is excessive heating in EEG electrodes due to current induction from the interaction between EEG electrodes and the attached wire [17].

After several years of developing simultaneous EEG-fMRI techniques, safety issues can now be sufficiently addressed [18]. The careful design of EEG equipment can avoid any EEG interaction with the static and rotating magnetic fields required for signal excitation and reception in fMRI acquisition. As such, no extra pre-processing is required for fMRI data after simultaneous recording with EEG [19, 20]. However, recording EEG inside the scanner and acquiring EEG signals during fMRI acquisition results in EEG signal contamination from ballistocardiogram (BCG) and gradient artifacts, respectively. Physiological artifacts, such as blinking and muscle artifacts, contaminate the EEG data regardless of whether EEG is being recorded inside or outside the scanner.

Rapidly varying magnetic field gradients for spatial encoding of MR signal during fMRI acquisition induce gradient artifacts in the EEG signal [21]. Further, a Radiofrequency (RF) electromagnetic field applied during imaging for spin excitation induces noises in EEG data. Nonetheless, the frequency range of the RF pulses is outside the frequency range of conventional EEG amplifiers, resulting in significantly attenuated artifacts [21]. Gradient artifacts' amplitudes appear at a much higher rate than normal brain EEG signals (see Figure 2-1), and need to be reduced/removed in the first step. Average artifact subtraction (AAS) [22] and optimal basis sets (OBS) [23], which are based on generating a template for this artifact and then removing it, are the most common methods for removing gradient artifacts. Nowadays, an accurate and reproducible template of gradient artifacts can be obtained with high-quality MRI scanner gradient controllers and with the synchronization of EEG digitization with the MRI clock signal.

Such a template subtraction has proven to be extremely successful in reducing gradient artifacts [24].

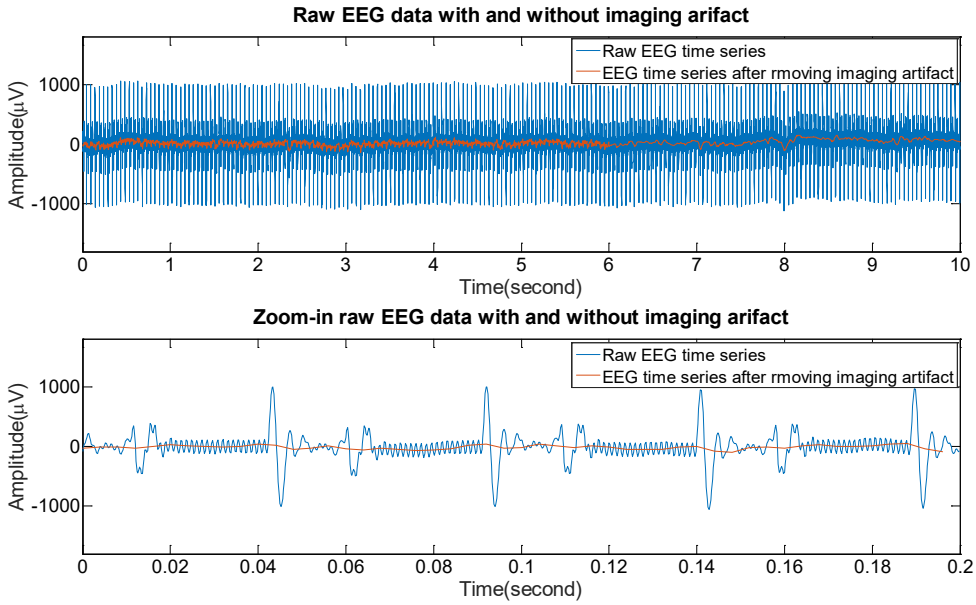

Figure 2-1: EEG time course with gradient artifact (sampled at 5000 S/s) and after reducing that artifact with average artifact subtraction (AAS) sampled at 250 S/s.

A BCG artifact obscures an EEG signal recorded inside the MRI scanner independent of MRI acquisition presence and significantly affects EEG quality. Based on Faraday's law, any movement of electrically-conductive material in a static magnetic field results in electromagnetic induction, which is the fundamental cause of a BCG artifact. In other words, motions related to cardiac activity induce electromotive forces in the circuit formed by the EEG recording leads and in the subject and thus contaminate the EEG data with the BCG artifact [21]. Reducing the BCG artifact is more challenging compared to gradient artifact and demands additional attention. First, the BCG artifact frequency range overlaps EEG spectra, especially theta and alpha rhythms. Second, determining a template for removing BCG artifacts using AAS or OBS is more challenging since BCG artifacts are the result of an interaction between the cardiovascular

system and the main static field inside the MRI, and of the added inter-subject and inter-recording variability. Using AAS to remove BCG artifacts requires precise Q wave, R wave, and S wave (QRS complex) detection. Third, the ECG signal recorded inside the MRI scanner contains artifacts, and sometimes detecting a precise QRS, which is required for both AAS and OBS, is not easy. Figure 2-2 shows an example of such an artifact on EEG data and the result of reducing it using AAS. The challenge associated with removing BCG will be discussed in greater detail in the next chapter.

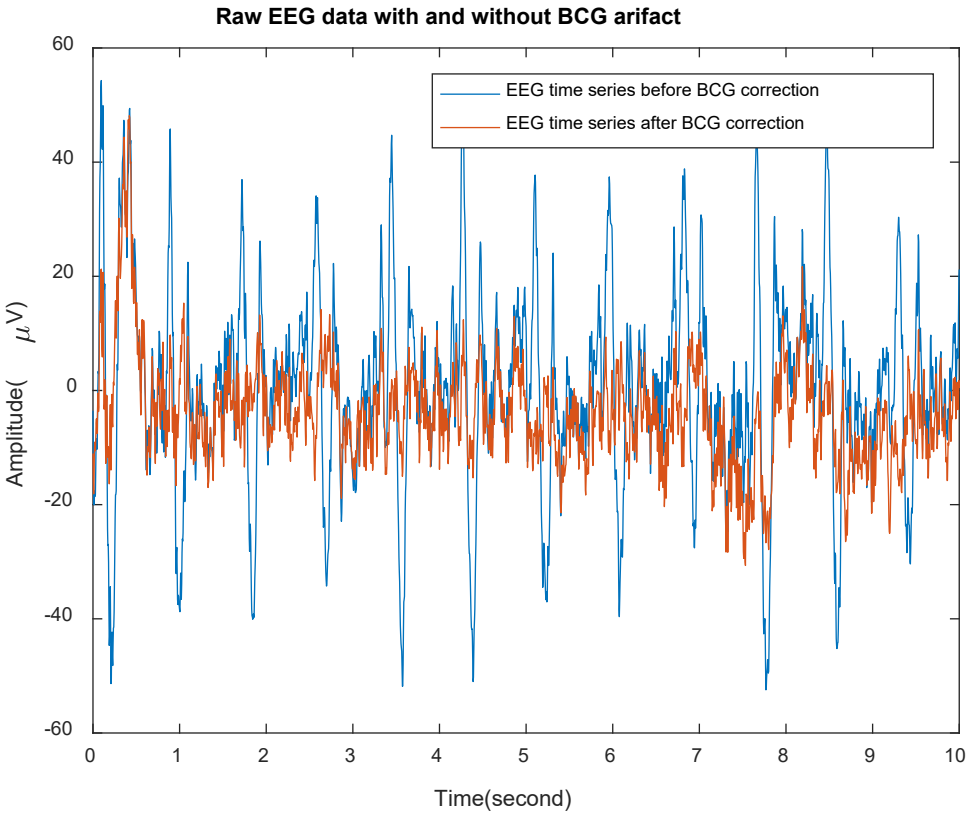

Figure 2-2: EEG time course with ballistocardiogram (BCG) artifact and its reduced artifact using average artifact subtraction (AAS) both sampled at 250 S/s.

2.5 Pupilometry

Pupillometry measures the spontaneous variation of pupil diameter and dilation due to light changes or mental effort and cognitive activity. Primarily, it is assumed that the pupil dimension is associated with the amount of cognitive control, attention, and cognitive processing required by a given task [25]. In the absence of any task (i.e., resting state), pupil dilation can be accounted for by the subject's vigilance and arousal. To find the EEG features associated with vigilance, an eye tracker was used for the study presented in Chapter 4.

Chapter 3: Automated Pipeline for EEG Artifact Reduction Recorded during fMRI (APPEAR)

3.1 Introduction

As mentioned in the previous chapter (section 2.4), recording EEG inside of an MRI scanner and acquiring EEG signals during fMRI acquisition results in EEG signal contamination from gradient and ballistocardiogram (BCG) artifacts, due to the switching of the magnetic field during fMRI acquisition and the presence of a static magnetic field (e.g., 3T) inside the scanner room. Other types of artifacts, such as muscle and ocular artifacts, can be present in EEG data regardless of whether the EEG is recorded inside or outside the MRI scanner [12, 26].

After years of developing simultaneous EEG-fMRI techniques, several methods have been proposed for reducing artifacts from EEG data based on three main strategies.

Firstly, making a template from BCG and gradient (i.e., MR-related artifacts) artifacts and then subtracting this template from the main signal [22, 23, 27, 28]. To date, the average artifact subtraction method (AAS) [22, 28] is one of the most common approaches for reducing BCG and gradient artifacts. The AAS method uses the repetitive pattern of gradient and BCG artifacts to generate an artifact template, which is then subtracted from the EEG signal. Even though the AAS can effectively reduce BCG and

gradient artifacts, some residual artifacts remain when this method is applied to raw EEG data in both real-time and offline [23, 29]. By leveraging high-quality MRI scanners and precise synchronization of MRI and EEG system clocks, we can generate accurate and reproducible templates of gradient artifacts, and AAS is shown to be extremely successful in reducing this type of artifact [24]. However, using AAS for reducing BCG artifacts requires additional consideration due to the artifact's variability. In other words, AAS assumes that BCG artifacts are stable over time; however, this is not always the case. BCG artifacts are known to fluctuate over time, resulting in excessive residual BCG artifacts when using AAS. Combining AAS with other approaches, such as independent component analysis (ICA), is one solution to remove the residual artifacts [30-32]. [23] suggested a more comprehensive approach based on AAS, namely the optimal basis set (OBS), for reducing MRI- related artifacts. To minimize the effect of residual gradient and BCG artifacts, they proposed using principal component analysis (PCA) for capturing temporal variations in artifacts and regressing them out from EEG data.

Secondly, using an extra sensor during recording simultaneous EEG-fMRI for capturing such artifacts and further subtracting them from the raw data [33-39]. A piezoelectric motion sensor was used by [33] to estimate motion artifact noise. The researchers calculated the correlation between the motion sensor and the EEG signal to further design a Kalman filter for removing BCG artifacts. [36] introduced a wire-loop-based technique for correction of motion and BCG artifacts. This method was adopted in real-time (van der Meer et al., 2016). [34, 35] suggested adding reference electrodes attached to a conductive reference layer to record artifacts and further remove them from

EEG data. Although those methods appear beneficial for reducing artifacts, they are not yet widely used due to required hardware modifications and additional equipment [40].

Thirdly, using blind source separation (BSS) for decomposing the EEG data into independent components and reconstructing the EEG data after removing artifactual independent components [26, 30, 41-46]. While AAS/OBS and using extra sensors have proven successful in reducing MR-related artifacts, these methods do not remove ocular, motion, and muscle artifacts. In contrast, BSS approaches are not recommended as the sole approach for reducing such artifacts but are often combined with OBS or AAS to remove residual MR and BCG artifacts. Using BSS as the primary method for reducing BCG is not suggested due to the difficulty of distinguishing BCG components from event-related ones [32, 47].

In this study, we proposed an automated pipeline for EEG artifact reduction recorded during fMRI (APPEAR). The APPEAR algorithm is an OBS/AAS-ICA-based algorithm for reducing BCG and gradient artifacts, in addition to motion, ocular, and muscle artifacts, in order to improve EEG data quality acquired during fMRI.

3.2 Methods

3.2.1 APPEAR

The APPEAR algorithm combines OBS/AAS, filtering, and ICA to reduce all types of artifacts contaminating EEG data due to simultaneous fMRI recording.

3.2.1.1 AAS/OBS and Filtering

Figure 3-1A shows the algorithm's first step and procedure for reducing noise and artifacts from EEG data. APPEAR first preprocessed raw simultaneous EEG-fMRI data by removing the gradient artifact using the OBS included in EEGLAB's FMRIB plugin and function fmrib_fastr [22, 23, 48]. The raw EEG data included the slice trigger markers (e.g., R128). Prior to running OBS, the volume start was added by setting the markers at every n^{th} occurrence of the slice trigger, in which n was equal to the number slices per volume. Volume trigger timing was used to generate an artifact template in OBS. After the removal of the gradient artifact, the data were down-sampled to a 250 S/s sampling rate (4 ms interval), and the EEG data was bandpass filtered between 1 and 70 Hz (0.1 and 70 Hz for task-based EEG data) using the built-in FIR filter in MATLAB named eegfilt. The fMRI slice selection frequency and its harmonics, vibration noise (26 Hz), and AC power line noise (60 Hz) were removed by band rejection filtering (1 Hz of bandwidth).

The AAS algorithm requires identifying the QRS complex in order to form the artifact subtraction templates [49]. For this purpose, two methods were attempted: **1-** the FMRIB plug-in for EEGLAB was implemented in MATLAB for QRS / Heart-Beat Detection using simultaneously recorded ECG data via the back electrode [23]; **2-** an automatic cardiac cycle determination approach using ICA [49]. Specifically, the ECG data recorded during fMRI acquisition is likely contaminated with MR environment artifacts. Thus, the identification of QRS events could be impractical or difficult to determine. Furthermore, any subject's movement affects the quality of the recorded ECG data. Therefore, the proposed automatic approach for detecting the cardiac cycle directly

from the EEG data using independent component analysis (ICA) presented by [49] was implemented. We used the same parameters reported in [49] to detect the ICs related to BCG and the QRS events. In this study, the ICA-based approach was primarily used to detect the cardiac cycle and demonstrated superior performance comparing to detection from ECG signal. As a quality check, the resultant heart rate from the ICA method and FMRIB heart-rate calculations were compared to the heart rate indexed by simultaneous physiological pulse oximetry waveforms. For each fMRI run, simultaneous physiological pulse oximetry was collected (with 40 Hz sampling frequency, using a photoplethysmograph with an infrared emitter placed under the pad of the subject's left index finger). The ECG signal from this device is not sensitive to contamination from MRI environment artifacts, so the heart rate could be accurately detected. However, due to a lower sampling rate, as compared to the ECG signal recorded using the back electrode, the physiological pulse oximetry signal is not ideal for detecting the QRS cycle and generating a pulse artifact template. We chose the QRS cycle detection method that had the closest average heart rate achieved by pulse oximetry for generating the pulse artifact template.

After detecting the heartbeat pulses, BCG artifacts were reduced using AAS, which is included in EEGLAB's FMRIB plugin. Although OBS outperformed AAS in several studies in removing BCG artifacts [50, 51] (as shown in Figure 3-2 for data from two different participants), OBS could potentially remove some neural activity. Therefore, we selected AAS as the template correction approach for BCG correction. After reducing the BCG artifact using AAS, the data were then examined for intervals

exhibiting significant motion or instrumental artifacts ("bad intervals") using EEGLAB's function, named pop_rejcont, and bad intervals were marked for removal.

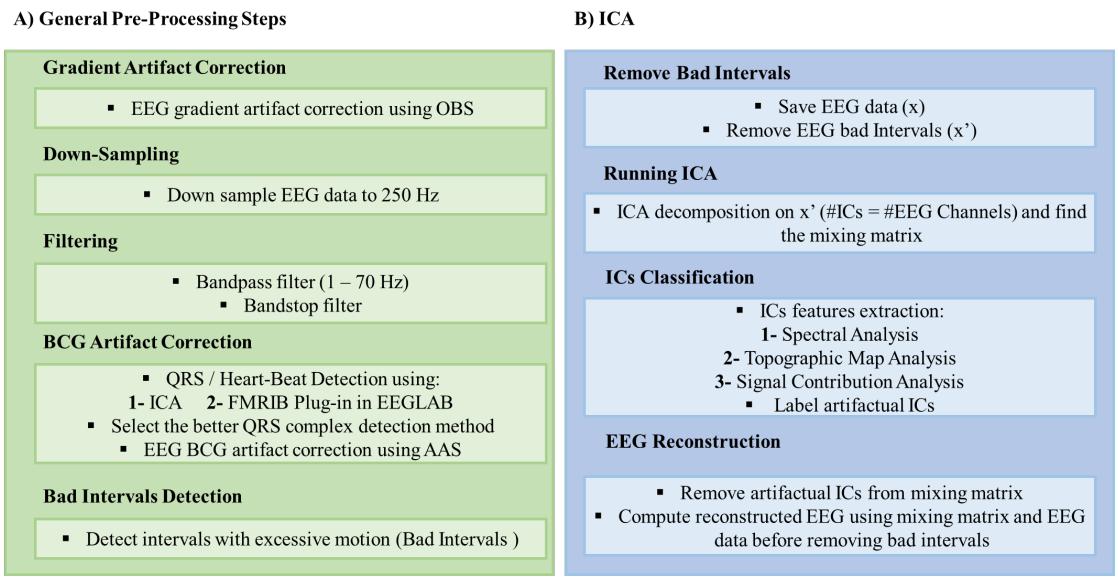

Figure 3-1: The APPEAR flowchart.

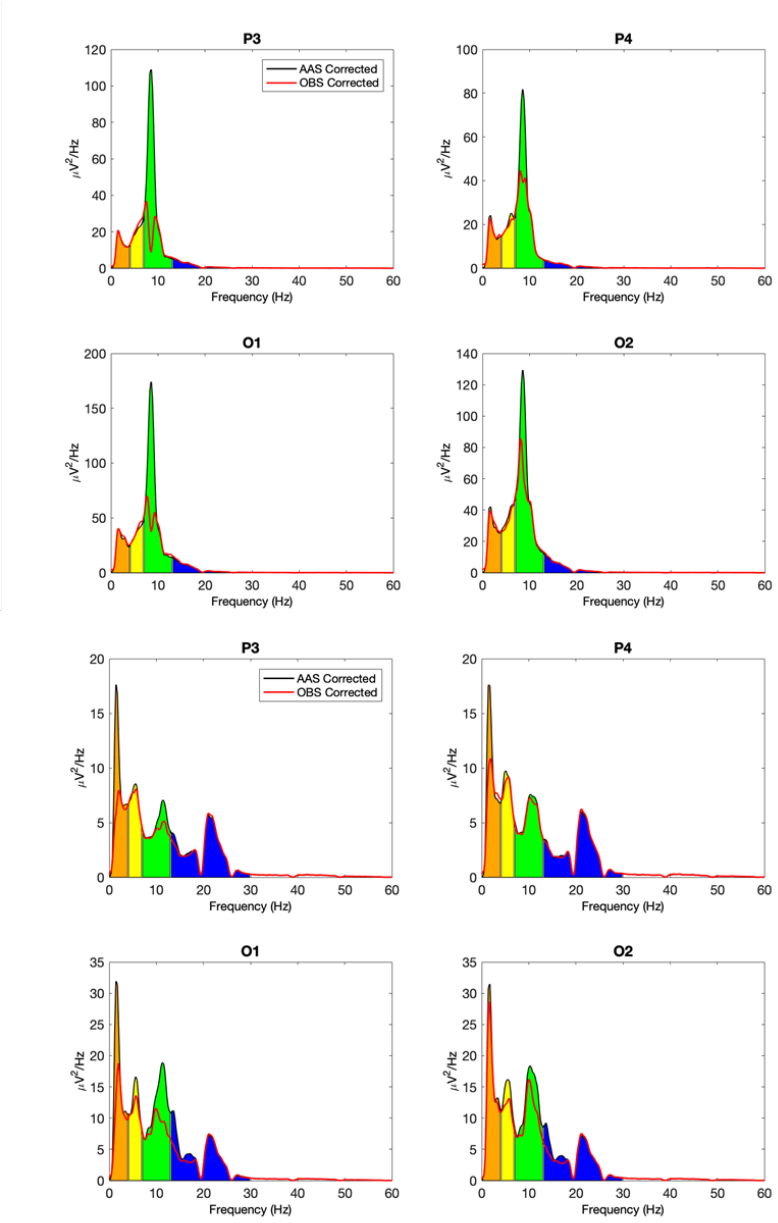

Figure 3-2: Comparison between power spectral density (PSD) after applying average artifact subtraction (AAS, black line) and optimal basis sets (OBS, red line).

3.2.1.2 ICA

The flowchart presented in Figure 3-1B illustrates the automatic artifact reduction using ICA after the preprocessing and removal of the gradient and BCG artifacts. The

Infomax ICA algorithm [52], implemented in the EEGLAB toolbox, was applied to the EEG data after template artifact correction. The ICA algorithm was used to decompose the (*N x M)* EEG data into (*L x M)* independent components (ICs), where *N, L*, and *M* denote, respectively, the number of channels, ICs to be estimated, and time-samples. The number of components was set to the number of EEG channels (31 for this study). The equation describing the relationship between the EEG data, **x**, and the independent components, **S**, is given by:

$$\boldsymbol{x}_{[N\ x\ M]} = \boldsymbol{A}_{[N\ x\ N]} \cdot \boldsymbol{S}_{[N\ x\ M]}$$

where **A** is the mixing matrix that carries the coefficients of the linear combination between the EEG data and the ICs [53]. Bad intervals could significantly affect the ICA results due to their high amplitude and power and were therefore removed prior to ICA, resulting in a new (*N x K)* matrix, **x'**. An ICA was applied, resulting in a new relationship between the shortened EEG data and the resulting ICs, **S'**, given by:

$$\boldsymbol{x'}_{[N\ x\ K]} = \boldsymbol{A}_{[N\ x\ N]} \cdot \boldsymbol{S'}_{[N\ x\ K]}$$

3.2.1.3 Automatic IC Classification

Independent components (ICs) were flagged within the APPEAR algorithm if they were determined to be one of the following artifacts: BCG, blink, saccade, single channel, or muscle. Artifacts are determined with spectrum properties, topographic map properties, or an analysis of each IC's contribution [54].

BCG IC Identification

BCG artifacts obscure EEG signals recorded inside the MRI scanner, independent of MRI acquisition presence, and significantly affect the quality of the EEG. These artifacts occur fundamentally because of Faraday's law, which states that any movement of electrically-conductive material in a static magnetic field results in electromagnetic induction. In other words, motion related to cardiac activity induces electromotive forces in the circuit formed by the EEG recording leads and the subject, which contaminate the EEG data with BCG artifacts [21]. ICs are flagged as BCG if they meet requirements for the mean power spectral density, topographic map, and IC contribution as follows [49, 54]. The parameters and threshold values were exactly adapted from [49]. The power spectrum is divided into two ranges, cardioballistic (2-7 Hz) and neuronal (8-12 Hz). If an IC has a cardioballistic artifact, the power spectrum shows peaks in both the cardioballistic and neuronal frequency ranges. The method used by [49] determines the rise of the peaks in both regions and requires that they meet four conditions to be considered a BCG artifact. Condition (i) states that a large peak must be present in the cardioballistic range; Condition (ii) states the rise of the neuronal peak (r_n) must be small; and if (ii) is not satisfied, then Conditions (iii) and (iv) define comparable spectrum amplitudes required in the cardioballistic and neuronal ranges for a BCG IC. For Condition (ii), the r_n is defined as the maximum power in the neuronal range. To obtain the full rise of the neuronal peak, a frequency range is defined with the frequency at the local minimum immediately below 8 Hz ($v_{1<}$). If such a local minimum exists, the frequency range is taken as $[v_{1<},v_p]$, where v_p is the peak frequency; otherwise, the

frequency range becomes [8 Hz, v_p]. The rise of the neuronal peak is taken as the difference between the $S(v_p)$ and the minimum power given within the above range.

$r_n = S(v_p) - \min(S(v), v \in [v_{1<}, v_p])$, if $v_{1<}$ exists

$r_n = S(v_p) - \min(S(v), v \in [8\text{ Hz}, v_p])$ if $v_{1<}$ does not exist

For Conditions (iii) and (iv), a baseline (S_{min}) is defined for each spectrum by the minimum power below the neuronal peak frequency. A cardioballistic motion IC is recognized when the mean power in the cardioballistic frequency range is comparable to the neuronal peak rise. There may be multiple peaks in the cardioballistic range, $i=1,\ldots,N_{bcg}$. Condition (iii) requires that the cardioballistic peaks have a local minimum on the left and a peak rise larger than $0.2S_0$. Condition (iv) requires that the maximum rise of the peaks in the cardioballistic range, or the mean power over the cardioballistic range, is sufficiently large compared to the neuronal peak rise. Condition (iv) is met if any of the following equations are met:

1) $r_n <= 0.33S_0$

2) For N_{bcg} cardioballistic peaks with local left minimum and $r_{bcg,k} > 0.2S_0$, where $k=1,\ldots,N_{bcg}$, $\max([r_{bcg,k}], k=1,\ldots,N_{bcg}) > r_n - 3$

3) For N_{bcg} cardioballistic peaks with local left minimum and $r_{bcg,k} > 0.2S_0$, where $k=1,\ldots,N_{bcg}$, $\text{mean}(S(v), v \in \text{cardioballistic range}) - S_{min} > 0.33r_n$, $\max([S_{bcg,k}], k=1,\ldots,N_{bcg}) > S_n - 3$

The spatial projection of each IC onto the EEG channel space forms a topographic map. The spatial projection vector is interpolated using the MATLAB function, griddata. Normally, BCG ICs exhibit opposite polarity in the left and right regions [55]. During the topographic map analysis, the radius and other values are normalized to the range of 0 to 1. Then, two sets of polarity regions, primary and secondary, are defined. [49] creates polarity arc regions, defined as the overlapping polarity regions using a topographic map boundary with a width of 0.2. Any regions not defined by the primary and secondary regions are labeled as neutral regions. Using the three conditions developed in [49], the BCG ICs are flagged. Condition (i) requires that there be up to one neutral region in the topographic map; Condition (ii) requires that only one positive (or negative) polarity region and polarity arc region are allowed in the topographic map; Condition (iii) ensures that there is a left/right opposite polarity region with one negative (or positive) primary polarity region and polarity arc region; and Condition (iv) sets the minimum areas for the secondary polarity and polarity arc regions in the topographic map.

In the time-series of a BCG IC, there are distinct peaks (~1 second) caused by cardiac pulsations. Removing the BCG IC from the EEG time-series signal shows a steady signal reduction at the pulsation peaks. Looking at the signal contribution of a BCG IC, the average positive and negative magnitudes (α_+ and α_-, respectively) of the reduced signal (α') after removing the IC are compared to the original time-series signal (α). In [49], the thresholds for the average positive and negative magnitudes for any channel j are: (i) $0.5(\alpha_{j+}'/\alpha_{j+} + \alpha_{j-}'/\alpha_{j-}) < 0.97$ and (ii) $\min(\alpha_{j+}'/\alpha_{j+} + \alpha_{j-}'/\alpha_{j-}) < 0.95$. If these two thresholds are met, the IC is flagged as a BCG artifact.

We slightly modified the protocol reported in [49, 54] for selecting the BCG components for removal so that no components were removed that showed strong alpha activity in the occipital electrodes. To do so, we defined a template that covered the occipital electrodes (O1, O2, and Oz). If the topographic map had an area overlap (more than 0.4 if unipolar, or 0.91 if bipolar) and if the highest value of the power spectral density (PSD) was in the alpha band range (i.e., 7 to 13 Hz), or if there was an average PSD in the alpha band that was higher than the delta, theta, and beta bands, we did not consider that component to be a BCG artifact. On the other hand, if the topographic map exhibited bipolar properties affecting the right and left hemisphere and had neither the maximum PSD in the alpha band nor the highest average PSD in the alpha band compared to the other EEG frequency bands, we considered that component a BCG artifact. Figure 3-3 shows an example of a BCG artifact's IC time series and its features.

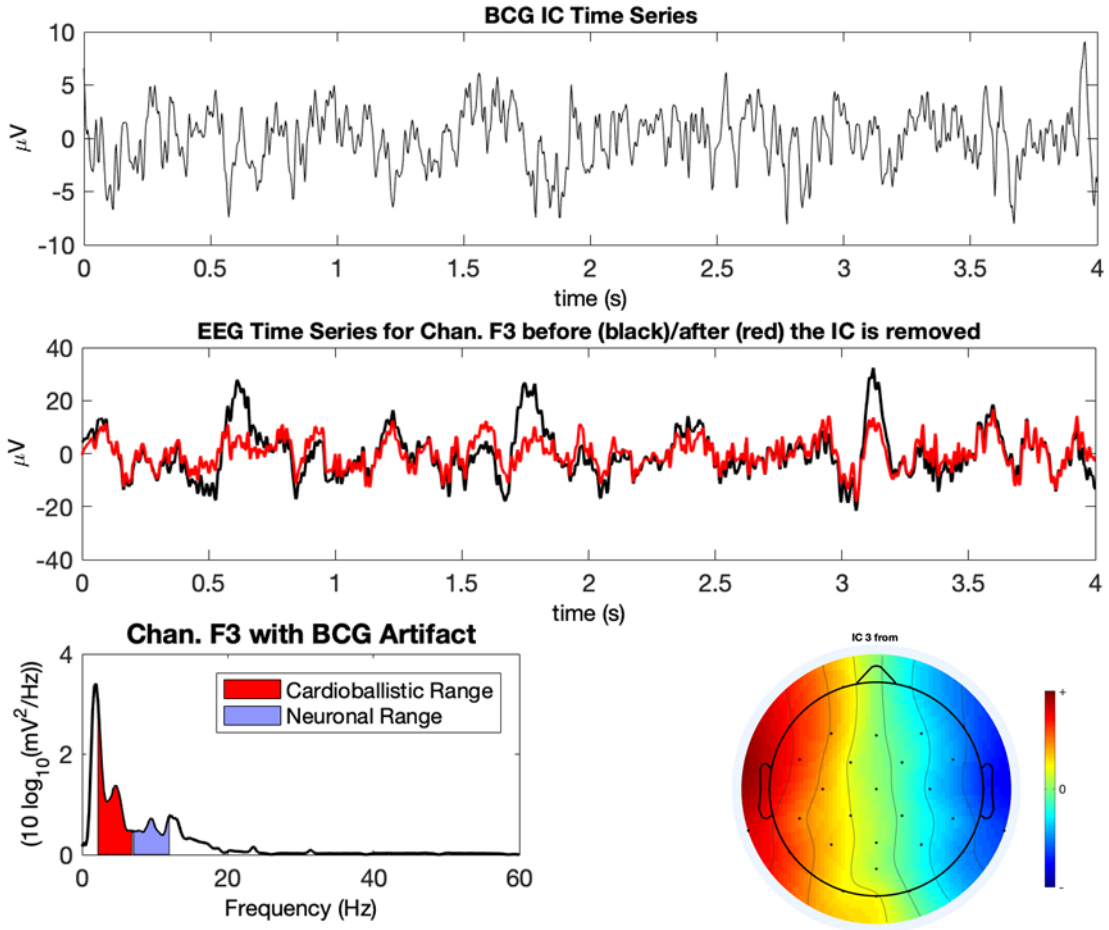

Figure 3-3: An Example of a ballistocardiogram (BCG) component.

Blink and Saccadic IC Identification

Ocular artifacts are separated into either blink or saccade (i.e., rapid movement of the eye between fixation points) components. The independent components associated with blinks, as well as saccade, have unique topographic maps. To detect the ICs with topographic maps related to blink and saccade, we used the approach presented in [54]. Blink ICs can be identified by their strong spatial projection in the frontal area; however, the topographic map related to saccade ICs depicts two strong and opposite polarity spatial projections behind the eye. The details of identifying the topographic map

associated with these two artifacts are presented in the supplementary material of [54]. Figure 3-4 shows an example of a blink artifact's IC time series and its features.

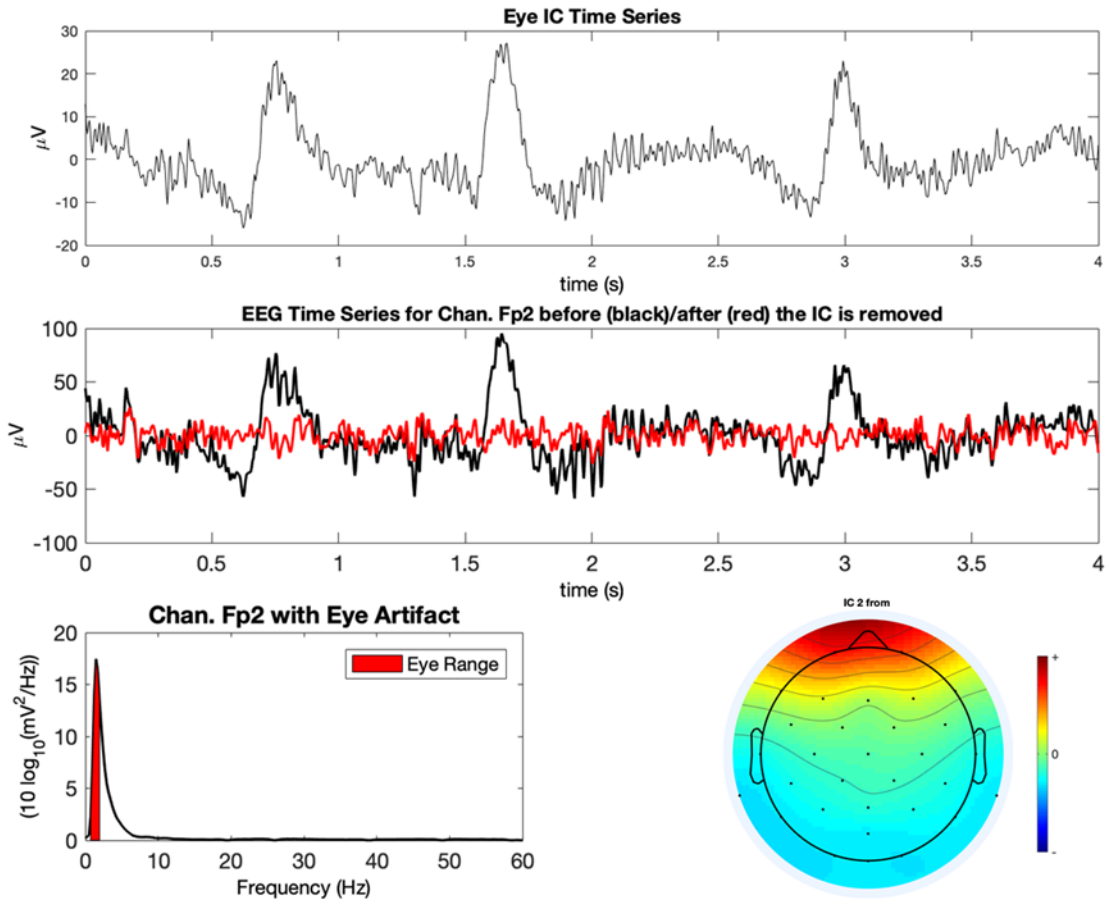

Figure 3-4: An example of a blink component. Blink ICs can be identified by their strong spatial projection in the frontal area and low frequency activity in delta band.

Single Channel IC Identification

A large artifact can be generated in one or two adjacent channels without affecting any other channels if that channel is bumped during a recording or if it has poor contact. Another reason these artifacts appear is that some EEG channels (e.g., T7, T8, TP9, and TP10) are more sensitive to jaw and head movement, which produce large artifacts for

those channels [41]. We call this type of artifact a single channel artifact. To determine if a component represents a single channel artifact, all ICs are removed except for the one being analyzed. The EEG signal is reconstructed with only the singular IC present, and then the power spectral density is computed for all 31 channels. The IC is flagged as a single channel artifact if it meets the following three requirements: (1) the power spectral density is large in only one channel,

$$max_1(PSD) > 5 \cdot max_2\ (PSD)\ \&\ max_1(PSD) > 10 \cdot max_3\ (PSD)$$

where the three maximum powers across all 31 channels are identified and sorted with max_1(PSD) being the largest power value, (2) the kurtosis is larger than 4, and (3) the average power is lowest in the narrow alpha band (8-12 Hz). An example of a single channel artifact's IC features is shown in Figure 3-5.

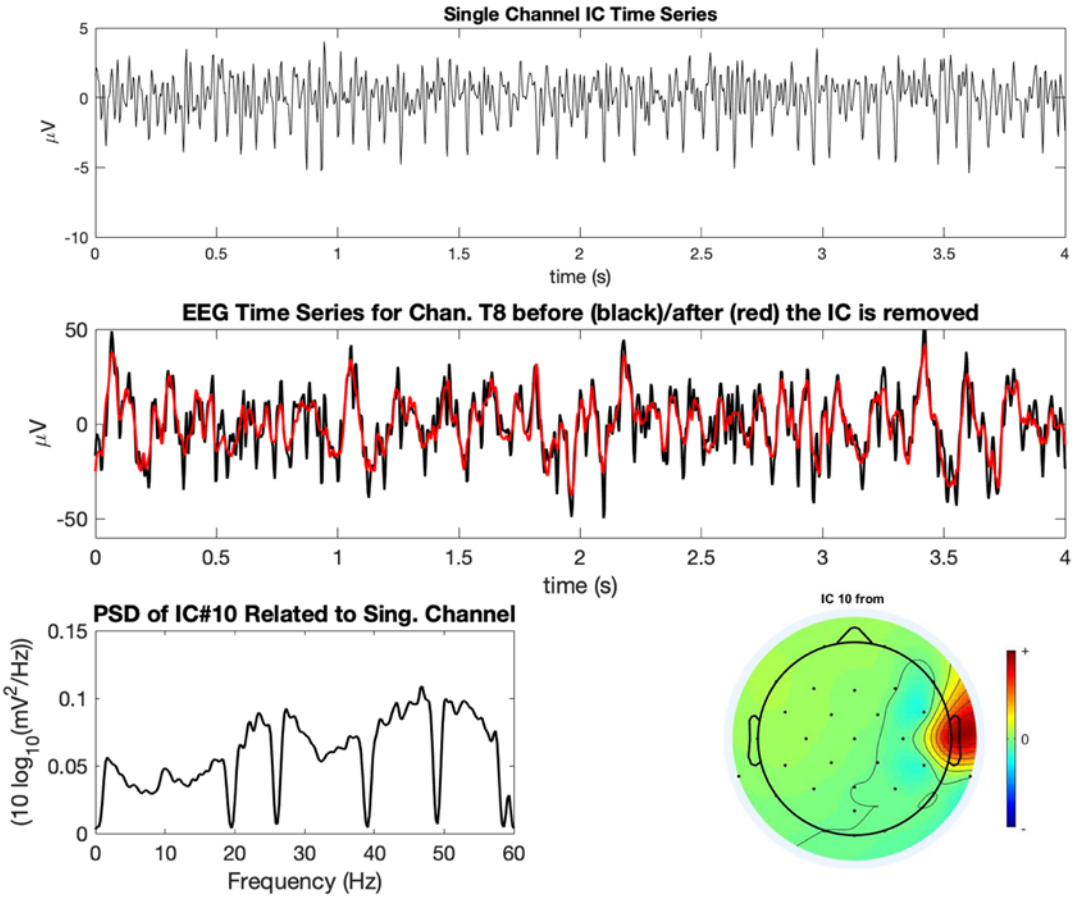

Figure 3-5: An example of a single channel component. This type of artifact affects mostly one or two electrodes due to either strong muscle activity around that electrode or to poor contact.

Muscle IC Identification

Muscle electrical activity or "electromyogenic" (EMG) artifacts exhibit widespread high-frequency activity due to asynchronous motor action units [12, 56]. These components are flagged if the power of the signal is spread out in frequencies higher than 30 Hz, known as the gamma band. Specifically, the average power of the gamma band is computed for each IC, and if the average power is largest in the 30-60 Hz range, the IC is labeled as a muscle artifact (see Figure 3-6 for an example of a muscle

artifact's IC features). Such classification considers possible components with a large peak in the gamma band, which typically represent some type of noise (e.g., vibration noise and line noise).

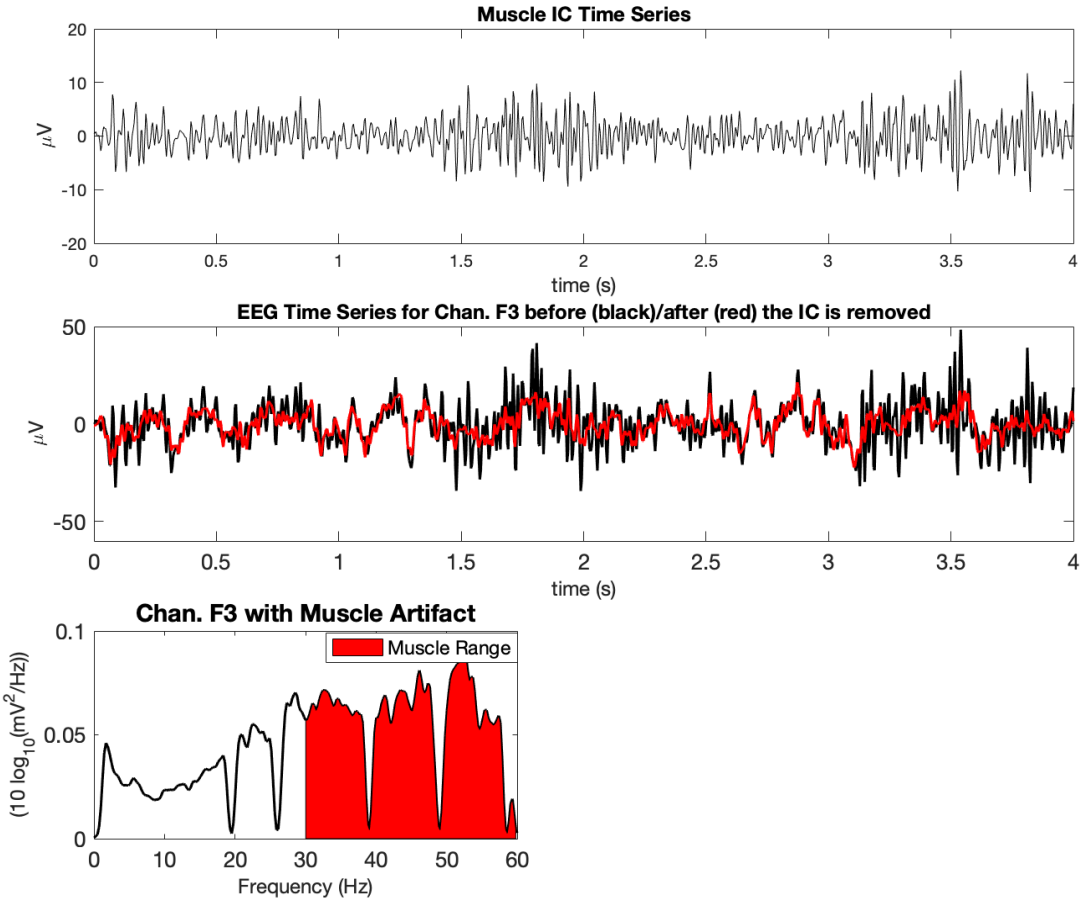

Figure 3-6: An Example of a muscle component. Muscle electrical activity or "electromyogenic" (EMG) artifacts exhibit widespread high-frequency activity due to asynchronous motor action units. These components are flagged if the power of the signal is spread out in frequencies higher than 30 Hz, known as the gamma band.

3.2.1.4 Reconstructing EEG Data after ICA Decomposition

Using the mixing matrix after the bad interval removal (i.e., "*A*") and the EEG data before the bad interval removal (i.e., "*x*"), the IC matrix related to the whole dataset (before removing bad intervals) was computed using the following matrix multiplication:

$$\boldsymbol{S}_{[N\ x\ M]} = \boldsymbol{A}^{-1}{}_{[N\ x\ N]} \cdot \boldsymbol{x}_{[N\ x\ M]}$$

The columns related to artifactual ICs were removed from the mixing matrix, A, and replaced with zero vectors to form a new mixing matrix, ***A'***. Then, a final, reconstructed EEG data matrix, $\boldsymbol{x}_{\boldsymbol{final}}$, with the same size as the original raw EEG, was computed using the original ICA relationship for EEG data and ICs, shown below:

$$\boldsymbol{x}_{\boldsymbol{final}\ [N\ x\ M]} = \boldsymbol{A}'_{[N\ x\ N]} \cdot \boldsymbol{S}_{[N\ x\ M]}$$

3.2.2 Data Acquisition

The data used for validation of the method was selected from the Tulsa 1000 (T-1000) study, which assessed and longitudinally tracked 1000 adults, including healthy comparisons and treatment-seeking individuals with mood and anxiety disorders [57]. We selected the first eight healthy control participants (8 females, age M = 26 years, range from 22 to 32 years) of that study. The study was conducted at the Laureate Institute for Brain Research with a research protocol approved by the Western Institutional Review Board (IRB). All volunteers provided written informed consent and received financial compensation for their time to participate in this study.

A General Electric (GE) Discovery MR750 whole-body 3T MRI scanner (GE Healthcare, Waukesha, Wisconsin, USA) and a standard 8-channel, receive-only head

coil array were used for fMRI imaging. A single-shot gradient-recalled echoplanar imaging (EPI) sequence with Sensitivity Encoding (SENSE) (Pruessmann et al., 1999) was used for fMRI acquisition (parameters: FOV/slice thickness/slice gap = 240/2.9/0.5 mm, 39 axial slices per volume, 128 × 128 acquisition matrix, repetition time (TR), echo time (TE) TR/TE= 2000/27 ms, acceleration factor R = 2, flip angle = 90°, sampling bandwidth = 250 kHz. EEG signals were recorded simultaneously with fMRI using a 32-channel MR-compatible EEG system from Brain Products GmbH. The EEG cap consisted of 32 channels, including references, arranged according to the international 10-20 system. One electrode was placed on the subject's back for recording the electrocardiogram (ECG) signal. A Brain Products SyncBox device was used to synchronize the EEG system clock with the 10 MHz MRI scanner clock. The EEG acquisition's temporal resolution was 0.2 ms (i.e., 16-bit 5 kS/s sampling), and measurement resolution was 0.1 μV. EEG signals were hardware-filtered throughout the acquisition in the frequency band between 0.016 Hz and 250 Hz.

3.2.3 Evaluation

APPEAR was validated using both an event-related-potential (ERP) and a resting-state EEG-fMRI dataset. We used manually-corrected EEG data as a comparison for evaluating the accuracy of the proposed automated pipeline for removing artifacts. We followed the method using template subtraction, followed by ICA, which was suggested for removing EEG artifacts in previous studies [26, 30, 32, 41, 47]. BrainVision Analyzer 2 software (Brain Products GmbH, Germany) was used to remove the artifacts manually and used the results of manual correction as a reference to evaluate the performance of APPEAR. The procedure for offline EEG artifact reduction was as follows [30]: **1-**

Imaging artifacts were reduced using the AAS method [22] and the signals were down-sampled to 250 S/s. **2-** Band-rejection filters (1 Hz bandwidth) were used to remove the fMRI slice selection fundamental frequency (i.e., 19.5 Hz) and its harmonics, vibration noise (26 Hz), and AC power line noise (60 Hz), and the EEG and ECG data were bandpass filtered from 0.1 to 80 Hz and 0.1 to 12 Hz (48 dB/octave), respectively. **3-** In order to remove the BCG artifact using AAS [28], the QRS cycle was automatically detected by the Analyzer 2 software with a subsequent visual inspection that corrected inaccurately positioned R-peak markers. A template of BCG artifacts from 21 preceding cardiac periods for each channel was used to remove BCG artifact using AAS. **4-** Prior to running ICA, the data were carefully examined to exclude the intervals exhibiting significant motion or instrumental artifacts. **5-** The *Infomax* algorithm [52] was used for ICA decomposition. ICs associated with artifacts were selected using the topographic map, power spectrum density, time course signal, and energy value. After selecting the artifactual ICs and removing them, the EEG signal was reconstructed using inverse ICA.

3.2.3.1 Stop Signal ERP

The first dataset was used to examine the quality of the corrected data was EEG-fMRI data during a stop signal task; lasting 8 minutes and 32 seconds. To determine the success of the pipeline in the separation and removal of BCG artifacts from EEG data, it is recommended that the quality of the signal of interest is examined [58]. Thus, examinations of event-related potentials extracted from the EEG data were used to evaluate the efficacy of the automated processing pipeline. Specifically, data resulting from the automated pipeline were compared to the same data processed manually as described above. For the ERP analysis, a commonly used paradigm (i.e., stop-signal; e.g.,

[59]) was employed. During this task participants were asked to respond to an "X" and "O" with either a right or left button press, but on 25% of the trials, an auditory tone (i.e., "stop-signal") indicated they should not respond. In this paradigm the stop-signal stimulus has been shown to elicit the N2 and P3 waveforms [60-62]. The N2 component is a negative deflection in the ERP waveform, maximal over the fronto-central portion of the scalp peaking between 200 and 250 ms (e.g. [63]), and is an indicator of attentional control. The P3 is a centro-parietally maximal positive deflection in the ERP waveform peaking between 300 and 500 ms and indexes attention allocation (see:[64]). In the current study, the eight participants completed the stop signal paradigm during simultaneous EEG/fMRI data collection, and the analysis was focused on the ERP response to a stop signal (72 trials).

In addition to the automated processing pipeline, the data were segmented from 200 ms prior to the 800 ms post onset of the stop signal. Then the data were baseline corrected to the average of the 200 ms interval preceding the stimulus onset. A low-pass filter was applied to the data with a half-amplitude cutoff of 30μv and 48dB/octave roll-off. Finally, automated routines were used to detect the bad intervals in the data. Bad intervals were defined as any change in amplitude between data points that exceeded 50μv; absolute fluctuations exceeded 200μv in any 200 ms interval of the segments (i.e., -200 to 800 ms); and flat-lining was defined as any change of less than 0.5μv in a 200 ms. Trials were excluded if they included any of these artifacts. The number of trials rejected due to above features ranged from 0 to 10 (M = 3.75, sd = 3.24).

According to recommendations from [58], we examined the scalp topographies, waveforms, and peak amplitude measures of the resulting ERP waveforms as well as the

estimated signal-to-noise ratio (SNR) of the N2 and P3 waveforms. The SNR of the ERP components was estimated in accordance with recommendations for processing EEG/ERP data [65, 66]. Specifically, SNR was calculated for two methods of quantifying ERP amplitude; peak amplitude (a measurement of the largest amplitude a waveform achieves in a specified measurement window) and grand average amplitude (average of the ERP waveform in a specified measurement window). This was done to account for common amplitude measures used in the field to compare groups and our conditions in ERP experiments. For peak amplitude, the SNR was calculated as the ratio of the ERP component peak and the difference between the largest negative peak and largest positive peak in the pre-stimulus baseline (estimate of noise). The grand average amplitude SNR was calculated as the ratio of mean amplitude measured across the following time windows, with respect to stimulus on-set: N2, 175-225ms; P3, 300-500ms over the baseline (i.e., -200-0ms) mean amplitude. All statistical analyses were conducted in R version 3.6.1 using the WRS2 package.

3.2.3.2 Resting-State

A resting-state EEG-fMRI run, lasting 8 minutes, was conducted for each subject. Prior to the rest run, participants were instructed to clear their minds, not think about anything in particular, and try to keep their eyes open and fixated onto a cross. In order to evaluate the resting-state EEG data quality using our proposed pipeline, we compared the time-frequency (Wavelet Transform), and frequency (FFT) results between the manually- and automatically-corrected EEG data.

The Continuous Wavelet Transform (CWT) was applied to the data after removing the average EEG signal among all channels (i.e., 31 channels). CWT deployed

the analytic Morse wavelet implemented in MATLAB's function cwt, with symmetry parameters of 3 and a time-bandwidth product of 60. To compare the results between the manually- and APPEAR-corrected EEG sets, we plotted the time-frequency analysis for only a 30-second segment of the EEG recording (for more visibility) taken from the 60 to 90 seconds.

In addition, we computed the power spectral density (PSD) for all EEG channels after AAS, for both the manual and APPEAR corrected data. To calculate the PSD in each analysis and channel, a moving window FFT, with 4.096 s data interval length (0.244 Hz spectral resolution) and 50% interval overlap with a Hanning window, was applied after the exclusion of the motion-affected intervals marked manually during the manual correction. After that, the PSD was averaged among all channels for each subject.

3.3 Results

Comparisons of the resulting ERP components between the APPEAR- and manually processed data are presented in Table 3-1 and Figure 3-7. Table 3-1 includes the means (M), standard deviation (SD), and statistical comparison (i.e., dependent samples t-test) of the means of the peak amplitude ERP components (i.e., N2, P3) between automated and manually corrected ERP data. Results indicate that there are no significant differences between peak amplitude ERPs calculated from data resulting from the automated pre-processing (i.e., APPEAR) and those calculated following manual pre-processing (uncorrected *p-values* range from 0.10 to 0.76).. It should be noted that, the N2 was quantified as the largest negative peak in midline channels (i.e., FZ, FCZ, CZ) between 175 and 225 ms post-stimulus onset based on a combination of visual inspections

of the current data and previous research indicating the N2 peaks between 200-250ms [63]. Notably, the N2 peak was not evident at PZ. The P3 was calculated as the largest positive peak between 300 and 500 ms post-stimulus onset at midline channels (i.e., FZ, FCZ, CZ, PZ). Figure 3-7 represents the ERP components waveforms and scalp topographies for both manually and automated corrected data.

Table 3-1. *T*-tests comparing mean amplitude N2, P3 across automated and manual processing.

N2		**Auto M(SD)**	**Man M(SD)**	**Mean comparison**
	Fz	-5.21(4.44)	-5.33(4.27)	$t(7) = 0.32$, $p = 0.76$
	FCz	-6.21(3.59)	-6.48(4.20)	$t(7) = 0.70$, $p = 0.50$
	Cz	-5.41(3.36)	-5.99(3.66)	$t(7) = 1.91$, $p = 0.10$
P3				
	Fz	8.45(4.79)	8.71(3.83)	$t(7) = -0.37$, $p = 0.72$
	FCz	11.51(5.81)	11.73(5.14)	$t(7) = -0.39$, $p = 0.71$
	Cz	11.69(5.34)	12.34(4.75)	$t(7) = -1.44$, $p = 0.19$
	Pz	9.03(3.86)	9.20(3.83)	$t(7) = -1.02$, $p = 0.34$

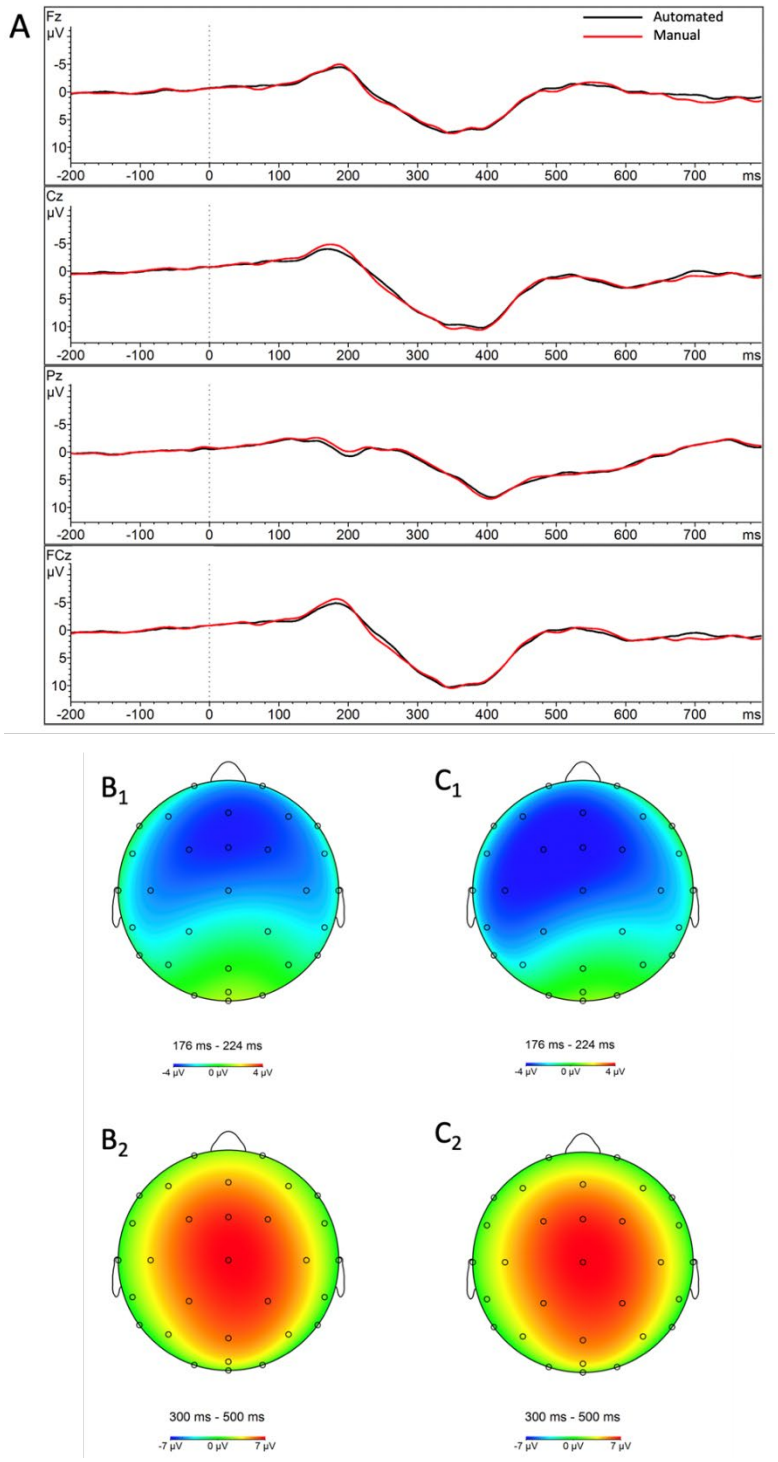

Figure 3-7: Comparison of waveforms (A) and topographical maps for ERP waveforms after applying APPEAR and manual correction (B1: N2 scalp topography from the automated correction; C1: N2 scalp topography from the manual correction; B2: P3 scalp topography from the automated correction; C2: P3 scalp topography from the manual correction).

Table 3-2 includes the mean, standard deviation, and statistical comparison (i.e., dependent samples t-test) of the SNRs of the peak amplitude ERP components (i.e., N2, P3). A series of dependent sample *t*-tests presented in Table 3-2 indicates that there were no significant differences between ERP components (i.e., N2, P3) resulting from the automatic processing compared to the manual processing (uncorrected *p-values* range from 0.20 to 0.97).

Table 3-2. *T*-tests comparing signal-to-noise ratios N2 and P3 across automated and manual processing.

N2		**Auto M(SD)**	**Man M(SD)**	**Mean comparison**
	Fz	2.15(1.39)	1.91(1.88)	$t(7) = -0.46$, $p = 0.66$
	FCz	2.38(1.34)	2.36(2.37)	$t(7) = -0.04$, $p = 0.97$
	Cz	2.03(1.41)	2.23(2.11)	$t(7) = 0.39$, $p = 0.71$
P3				
	Fz	3.80(2.25)	3.02(2.20)	$t(7) = 1.40$, $p = 0.20$
	FCz	4.67(1.43)	4.08(3.26)	$t(7) = 0.79$, $p = 0.45$
	Cz	4.58(2.61)	4.44(3.19)	$t(7) = 0.21$, $p = 0.84$
	Pz	3.53(2.74)	3.79(2.33)	$t(7) = -0.68$, $p = 0.51$

Table 3-3 and Table 3-4 show the SNR values for individual subjects for N2 and P3 (as the difference between the ERP peak amplitude measurement and the noise calculated in the baseline).

Table 3-3. Signal-to-noise ratios by individual subjects for the N2 Automated

	Fz	Cz	Pz	FCz
Subject 1	1.418	0.544	0.423	1.584
Subject 2	0.285	1.088	1.621	0.639
Subject 3	3.324	4.457	0.489	4.413
Subject 4	2.871	0.391	0.18	2.196
Subject 5	1.428	2.054	1.728	1.694
Subject 6	4.39	2.809	0.102	3.586
Subject 7	2.697	3.227	1.442	3.663
Subject 8	0.827	1.667	1.226	1.274
Mean	2.155	2.03	0.751	2.381
SD	1.389	1.406	0.858	1.343

Table 3-4. Signal-to-noise ratios by individual subjects for the P3 Automated

	Fz	Cz	Pz	FCz
Subject 1	4.345	3.661	3.311	4.934
Subject 2	0.381	1.399	1.76	0.967
Subject 3	5.25	8.884	4.318	8.065
Subject 4	6.062	4.411	2.95	5.852
Subject 5	2.565	3.828	3.18	3.55
Subject 6	3.73	3.919	1.903	3.99
Subject 7	6.757	8.102	5.717	8.43
Subject 8	1.337	2.423	5.158	1.531
Mean	3.803	4.578	3.537	4.665
SD	2.253	2.607	1.431	2.736

Table 3-5 represents the estimated SNRs of the mean amplitude measurements from the grand average across subjects of the N2 and P3 waveforms (i.e., N2, 175-225ms; P3, 300-500ms, post stimulus onset).

Table 3-5. Signal to noise ratios in the grand average waveforms.

Automated	**Fz**	**Cz**	**Pz**	**FCz**
GA Peak N2	4.279	3.194	0.767	3.822
GA Peak P3	7.029	8.306	7.565	8.081
GA Mean N2	3.266	2.053	0.16	2.904
GA Mean P3	4.342	5.735	4.838	5.232
Manual				
GA Peak N2	5.128	3.556	1.028	4.046
GA Peak P3	7.741	7.787	5.794	7.442
GA Mean N2	3.597	2.308	0.378	2.853
GA Mean P3	4.577	5.296	3.595	4.628

Table 3-6 and Table 3-7 show the individual grand average waveform SNRs for N2 and P3, respectively.

Table 3-6. Signal-to-noise ratios by individual subjects for the N2 Manual in the grand average waveforms

	Fz	Cz	Pz	FCz
Subject 1	1.631	0.711	0.105	1.645
Subject 2	0.351	0.841	1.374	0.62
Subject 3	1.691	2.987	0.926	2.664
Subject 4	0.305	0.079	0.015	0.072
Subject 5	0.88	1.771	1.343	1.263
Subject 6	4.438	2.778	0.211	3.764
Subject 7	5.211	6.811	2.467	7.47
Subject 8	0.803	1.879	1.961	1.361
Mean	1.914	2.232	1.02	2.357
SD	1.879	2.106	0.942	2.365

Table 3-7. Signal-to-noise ratios by individual subjects for the P3 Manual in the grand average waveforms.

	Fz	Cz	Pz	FCz
Subject 1	3.764	3.821	2.988	4.521
Subject 2	0.924	1.413	1.506	1.288
Subject 3	3.398	5.739	4.526	4.601
Subject 4	2.006	3.294	3.122	2.634
Subject 5	1.802	3.221	2.118	2.773
Subject 6	3.44	3.519	1.842	3.81
Subject 7	7.747	11.748	8.204	11.531
Subject 8	1.096	2.731	6.028	1.501
Mean	3.022	4.436	3.792	4.082
SD	2.198	3.19	2.328	3.258

Figure 3-8 shows the comparison between CWT results from APPEAR and manually corrected data.

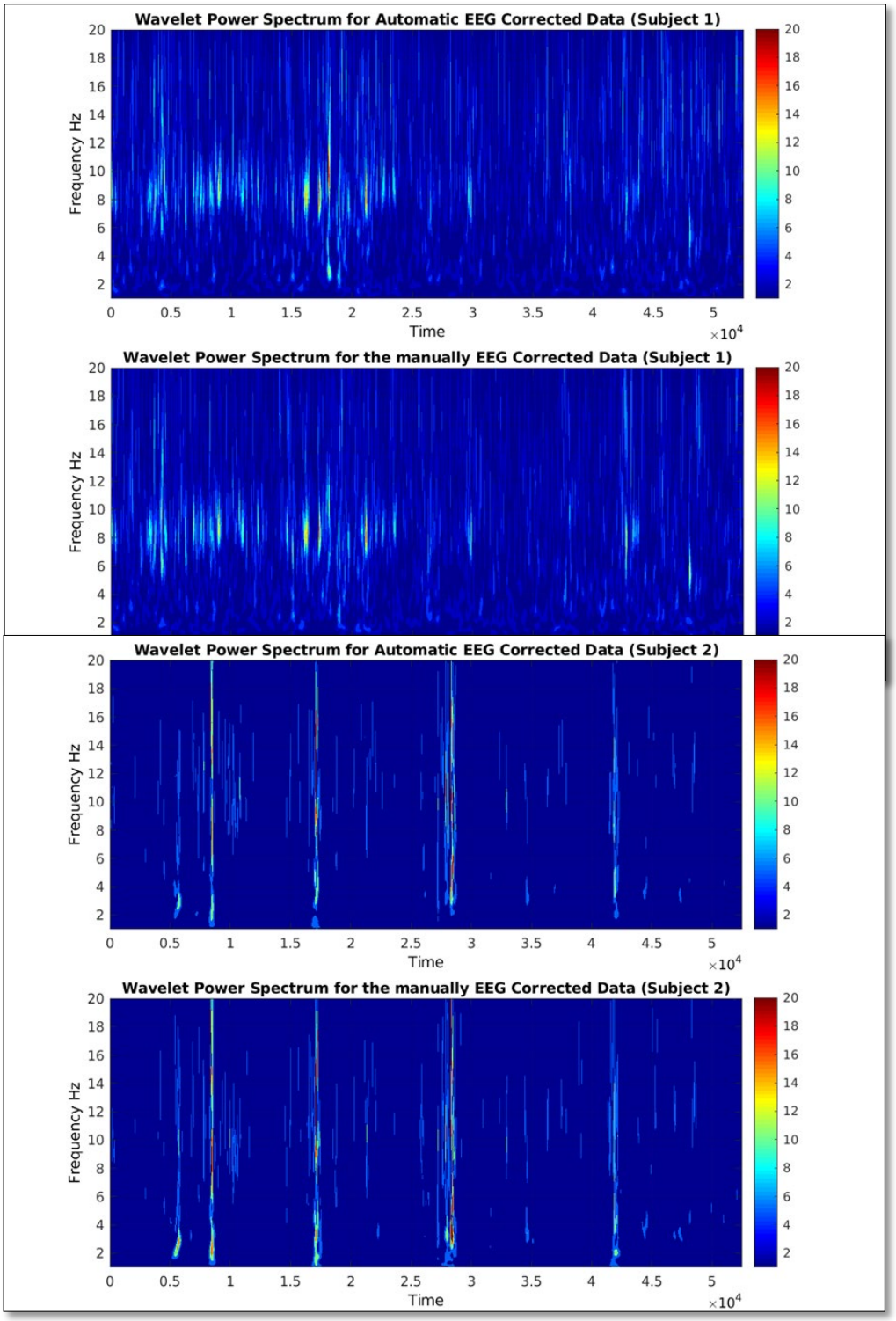

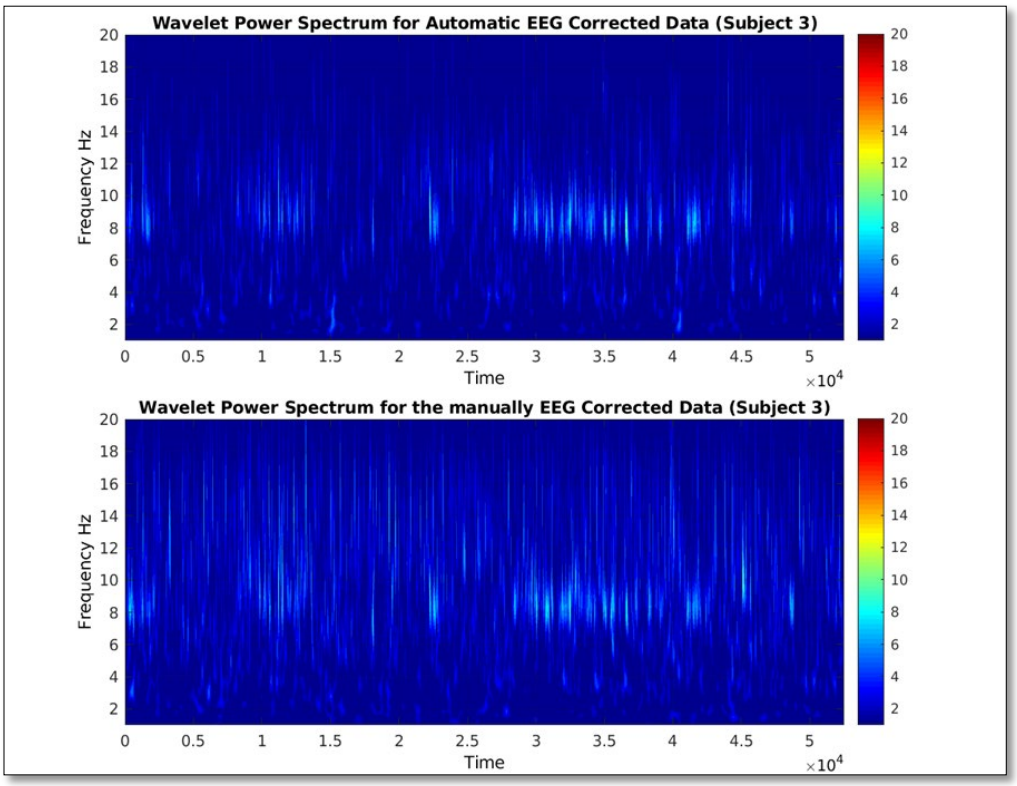
Wavelet Power Spectrum for Automatic EEG Corrected Data (Subject 3)
Frequency Hz
Time
×10^4
Wavelet Power Spectrum for the manually EEG Corrected Data (Subject 3)
Frequency Hz
Time
×10^4

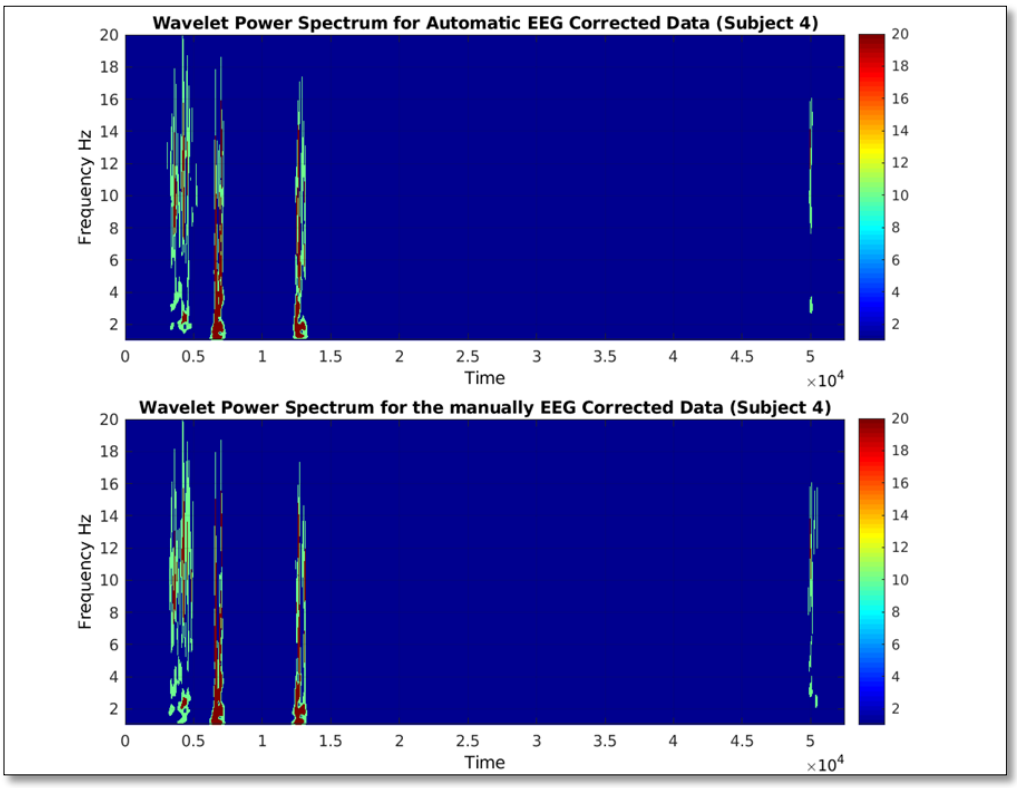
Wavelet Power Spectrum for Automatic EEG Corrected Data (Subject 4)
Frequency Hz
Time
×10^4
Wavelet Power Spectrum for the manually EEG Corrected Data (Subject 4)
Frequency Hz
Time
×10^4

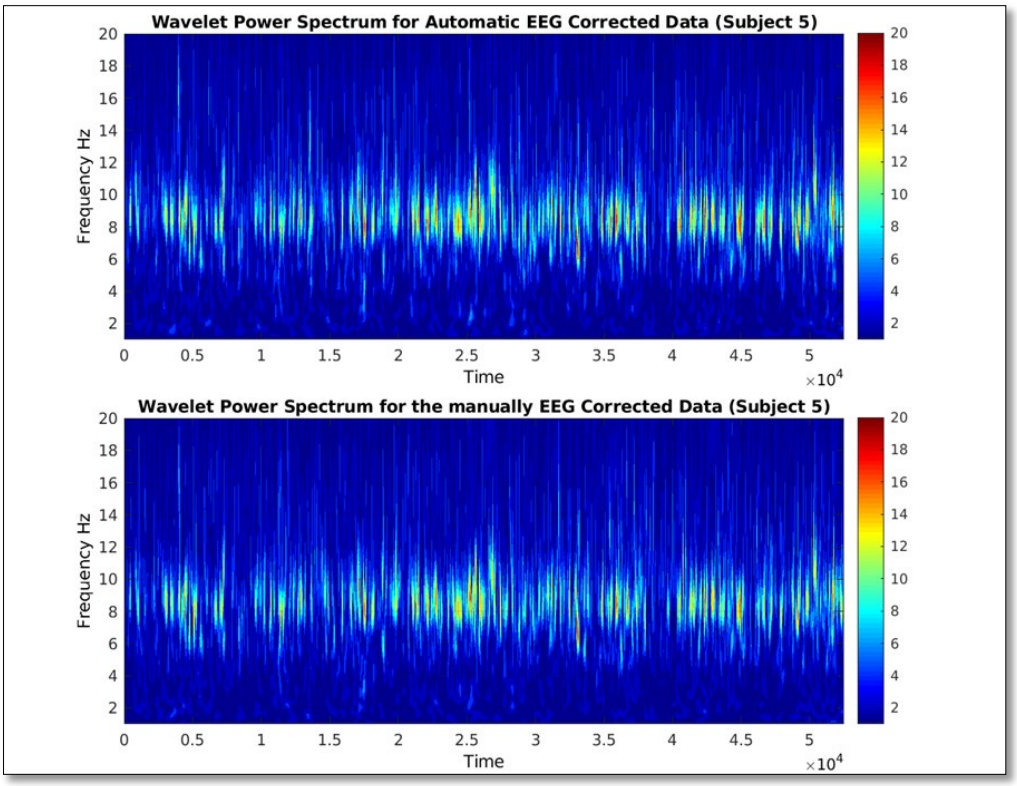
Wavelet Power Spectrum for Automatic EEG Corrected Data (Subject 5)
Frequency Hz
Time
×10^4
Wavelet Power Spectrum for the manually EEG Corrected Data (Subject 5)
Frequency Hz
Time
×10^4

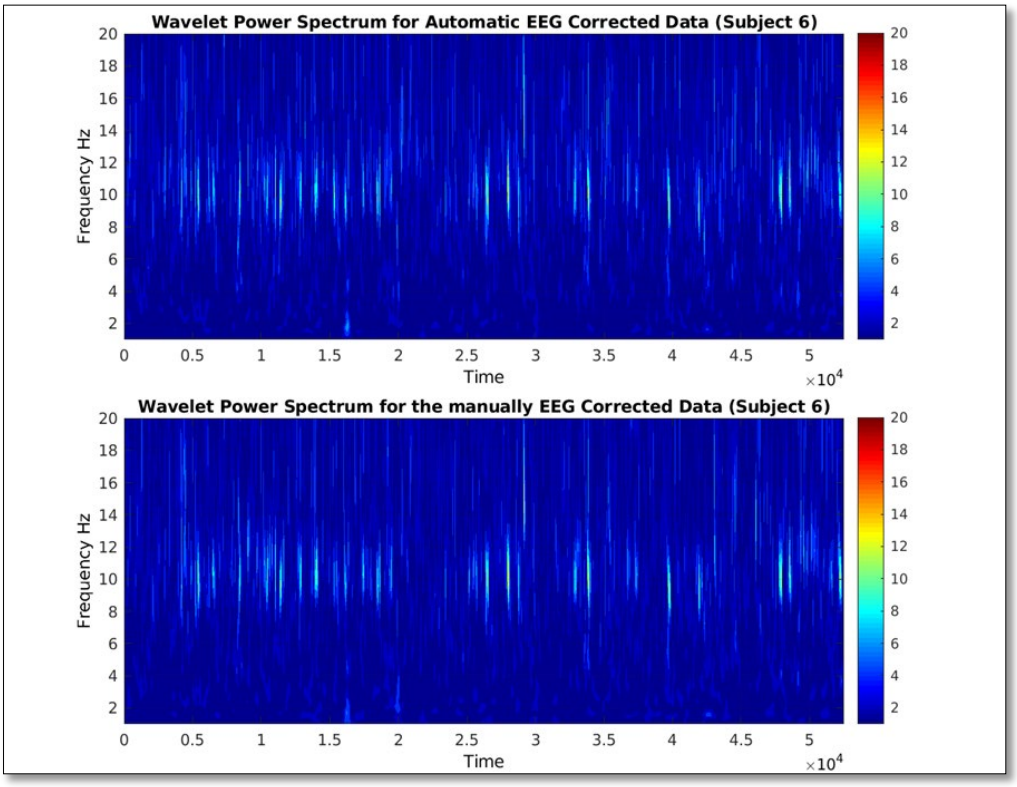
Wavelet Power Spectrum for Automatic EEG Corrected Data (Subject 6)
Frequency Hz
Time
×10^4
Wavelet Power Spectrum for the manually EEG Corrected Data (Subject 6)
Frequency Hz
Time
×10^4

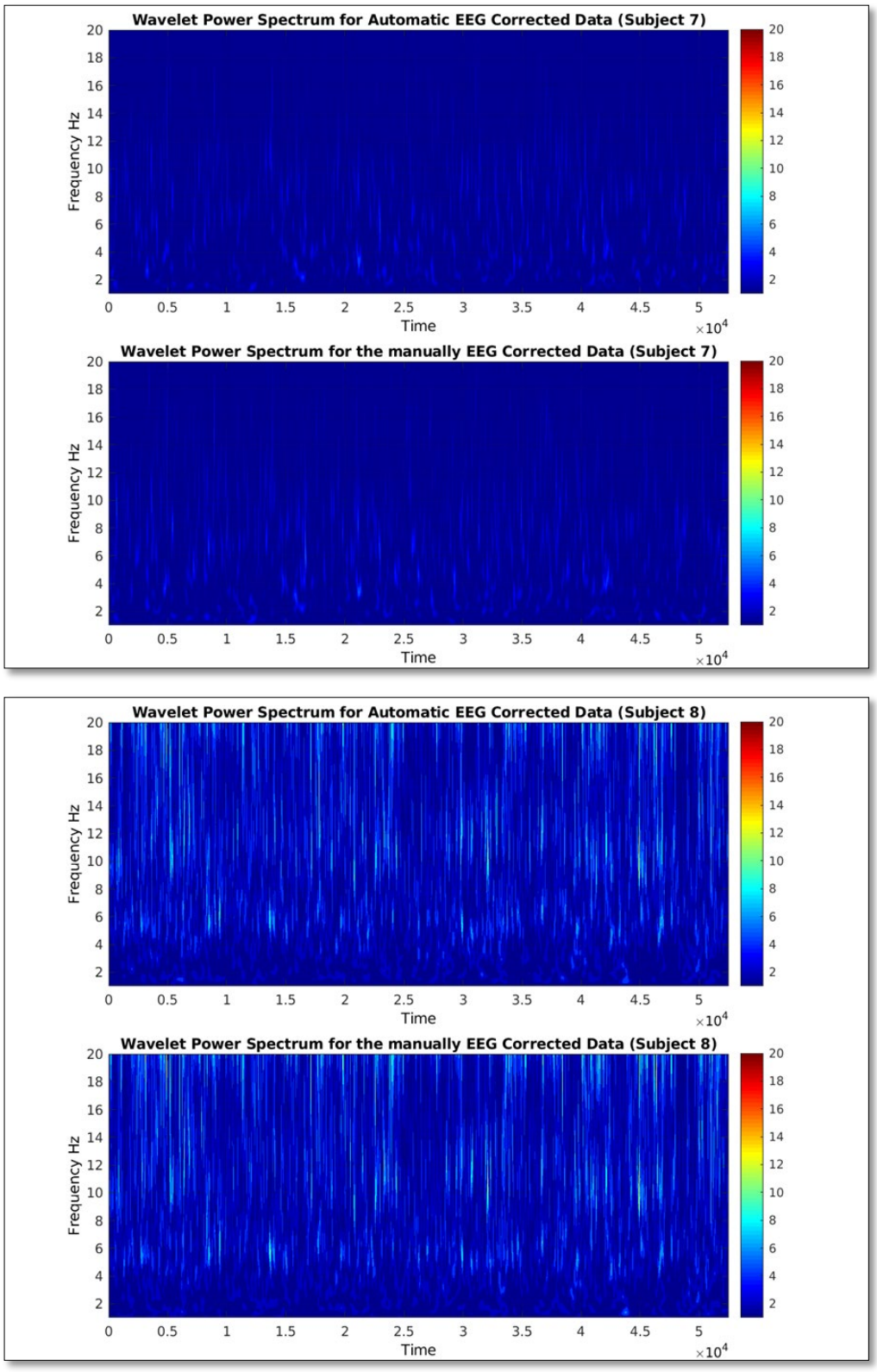

Figure 3-8: The time/frequency comparison (Wavelet) between APPEAR (upper rows) and manually-corrected EEG data (lower rows) for all individual subjects.

We also compared the PSD (averaged among all channels) in different frequency bands between the APPEAR and manually corrected EEG using a t-test. The results are as follows (Figure 3-9): Delta band: *t(7)= 0.1308*, *p= 0.8978*; Theta Band: *t(7)= 0.3124*, *p= 0.7594*; Alpha band: *t(7)= 0.1794*, *p= 0.8602*; Beta Band*: t(7)= -0.1375*, *p= 0.8926.*

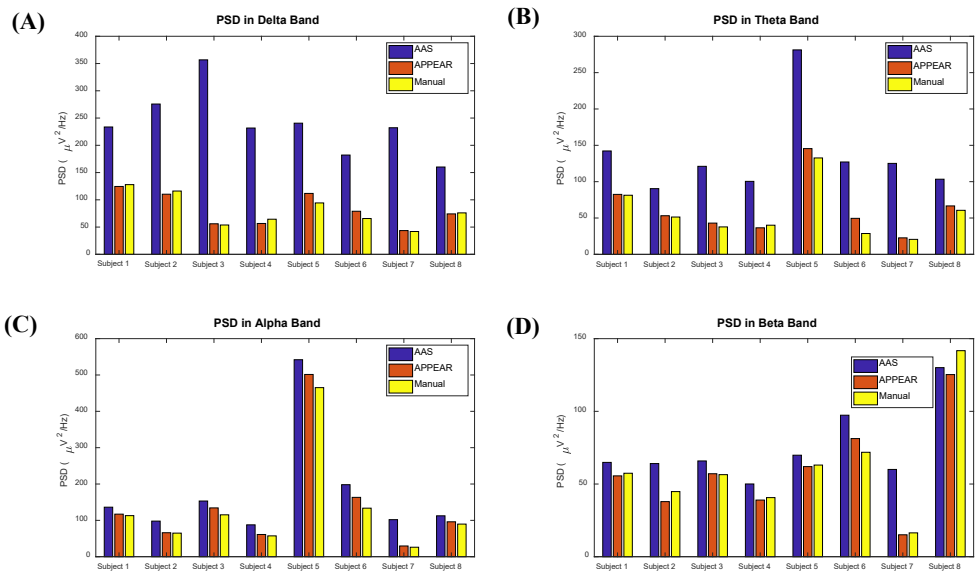

Figure 3-9: Powers spectral density (PSD) comparison between AAS, APPEAR, and manually corrected EEG data in (A) Delta; (B) Theta; (C) Alpha; and (D) Beta band.

3.4 Conclusion

Reducing MRI environment artifacts

Reducing gradient and BCG artifacts is the first step of artifact correction for any EEG data recorded during fMRI acquisition. To do this, we first reduced gradient and BCG artifacts using a template artifact correction. In the current study, we noticed a drawback in using OBS instead of AAS. Figure 3-2 illustrates important caveats in using OBS as an average template subtraction method, as it removed some neural activity (e.g., alpha wave in posterior and occipital channels). Therefore, we employed AAS for

reducing BCG artifacts instead of OBS. Furthermore, detecting the QRS cycle is still a challenge in using template artifact subtraction methods and could influence the efficacy of removing artifacts significantly with either aforementioned method. To have the best possible estimate of the QRS cycles, we used a newly-developed technique for detecting the QRS cycle using ICA on EEG data. This approach generally outperforms the FMRIB plug-in implemented in MATLAB for QRS cycle detection. However, we confirmed the estimation of the QRS cycle using the pulse oximeter waveform (which is unaffected by MRI environment artifacts). If the ICA method could not detect the QRS cycle accurately, we used the fMRIB approach using the ECG signal recorded via a back electrode.

Automatic Classification of Artifactual ICs after ICA Decomposition

Classifying the independent components may be the most difficult step in removing EEG artifacts, regardless of being recorded inside or outside the scanner. Although several methods have been proposed for automatic/semi-automatic IC classification for EEG data recorded outside the MRI [56, 67-72], there are very few for EEG data recorded inside the scanner [30, 73]. Here, in this study, we classified the components either as artifacts or neural activities. IC classification was determined with spectrum properties, topographic map properties, or an analysis of each IC's contribution. Using those features, we removed the ICs associated with residual BCG, ocular, muscle, and single-channel artifacts.

Evaluation

In this study, we validated our pipeline performance for two common applications of simultaneous EEG-fMRI (i.e., resting-state and ERP). For resting-state, we compared the wavelet transform, and FFT results between the manually corrected and APPEAR corrected EEG data. Our results showed no differences between the two approaches. The observed time course and scalp topographies (see: Figure 3-7) are similar to prior research examining the N2 and P3 in the stop signal paradigm (e.g., [60-62]) as well as the manually-corrected results.

Removing EEG artifacts remains one of the main challenges for simultaneous EEG-fMRI acquisition, due to its time-consuming nature and required special expertise. We developed a fully automated pipeline for reducing EEG artifacts and validated our results with two common applications of this multimodal acquisition. Our work represents an important step towards expanding EEG-fMRI applications by providing a faster and non-human biased method of removing EEG artifacts.

Chapter 4: Integration of Simultaneous Resting-State EEG, fMRI, and Eye Tracker Methods to Determine and Verify Vigilance Metrics

4.1 Introduction

Resting-state functional magnetic resonance imaging (rsfMRI) has become an important tool for studying the human brain due to its simplicity and non-invasiveness, as well as its requisite of least effort from the subjects [74-76]. rsfMRI scans are conducted while subjects have eyes-closed, eyes-open, or eyes fixated on a cross. Cross fixation is most often used and produces the most reliable results [77, 78]. However, it is unclear how well individuals manage to keep their eyes open and their gaze on the fixated cross over time using this paradigm. In addition, an individual's degree of changes in vigilance during rsfMRI may affect functional connectivity results in both the cortical and subcortical brain regions [79]. Therefore, to obtain a measure of vigilance during rsfMRI scans, employing another modality, such as eye-tracking or electroencephalography (EEG), is necessary. Independent and concurrent modality signals could then be used to continuously characterize one's fluctuations in vigilance, allowing researchers to use this vigilance index to better assess fMRI data quality. Notably, vigilance is a term that has been used in varying definitions by different groups

of scientists [80, 81]. For example, some groups consider it the ability to sustain attention to a task for a period of time [82, 83] and attention to potential threats or dangers [84]. One of the most common definitions for vigilance is tonic alertness [85-87], which is the definition adopted in this study.

EEG is the modality most extensively used for monitoring vigilance, specifically during eyes-closed resting states [5, 88-92]. Slow-wave EEG is mostly studied during sleep [7, 93], since delta (<4 Hz) and theta (4–7 Hz) waves dominate the EEG signal during drowsiness and sleep [93]. In contrast, alpha (7-13 Hz) and beta (13-30 Hz) rhythms and the ratio of high- to low-frequency band power have been employed to measure vigilance levels during resting states as well as during active tasks [89, 94, 95]. For instance, according to [88] three defined vigilance states based on EEG frequency characteristics during an eyes-closed rsfMRI recording exist: (1) alertness and relaxed wakefulness, characterized by dominant alpha activity; (2) drowsiness, classified by dissolving alpha activity and theta rhythm dominance; and (3) sleep, marked by slow-wave activity and sleep spindles. Further, this work [44], validated the results of the EEG vigilance classification by analyzing the heart rates during the different brain states [5]. When these EEG vigilance states were correlated with simultaneously recorded rsfMRI data, findings demonstrated that decreased vigilance was linked to a higher blood-oxygen-level-dependent (BOLD) signal in the parietal/occipital cortices as well as in regions of the prefrontal and anterior cingulate cortices (PFC and ACC). In addition, decreased vigilance was associated with reduced BOLD signal within the thalamus as well as in other specific regions of the PFC [5]. An additional eyes-closed rsfMRI study recording simultaneous EEG [89] introduced global field power (GFP) of the upper alpha

band (10 –12 Hz) oscillations as the most consistent EEG index of tonic alertness. Moreover, the GFP time course of the upper alpha band positively correlated with BOLD signal fluctuations within the dorsal ACC, anterior insula, anterior PFC, and thalamus. Given that eyes-closed and eyes-open conditions provide divergent EEG measures of vigilance with respect to brain topography and power [96] as well as differing BOLD signal patterns [77, 97-99], EEG vigilance measures used for eyes-closed resting states may not easily be applied to eyes-open paradigms.

One potential solution for monitoring vigilance during eyes-open rsfMRI is the use of an eye-tracker device to evaluate pupillometry [86, 100, 101]. The mean pupil diameter decreases during drowsiness [80, 102, 103], due to low tonic firing rates of the locus coeruleus neurons and dominant parasympathetic nerve system of the pupil [104, 105]. Although eye-tracker systems may have a relatively less complicated setup (and data post-processing), simultaneous EEG and fMRI recordings are more widely used to study brain functions than simultaneous eye-tracking and fMRI recordings. Therefore, we aimed to robustly derive and independently verify vigilance measures obtained from EEG data acquired during rsfMRI and to validate them with simultaneously collected eye-tracker and heart rate data.

To replicate and extend prior rsfMRI vigilance findings, the present study recorded simultaneous eyes-open rsfMRI, EEG, eye-tracking, and heart rate signals from healthy participants. First, we determined EEG features associated with pupil dimension and validated these features by correlating them with heart rate changes associated with arousal. Then, we investigated the relationship between these validated EEG features and

BOLD fMRI signals to illustrate the spatial and temporal characteristics of the brain's vigilance response.

4.2 Data Collection

This study was conducted at the Laureate Institute for Brain Research with a research protocol approved by the Western Institutional Review Board (IRB). Although 14 healthy subjects participated in this study, data from four volunteers were excluded due to excessive head motion, falling asleep, or closing their eyes during rsfMRI recording. Therefore, data from 10 participants (4 female, age M = 23.0 years, range 19-30 years) were analyzed. All participants provided written informed consent and received financial compensation for participation. Three 12-minute eyes-open rsfMRI runs were collected from each participant. Prior to each run, participants were instructed to clear their minds, not think about anything in particular, and try to keep their eyes open and fixated on the cross.

A General Electric (GE) Discovery MR750 whole-body 3T MRI scanner (GE Healthcare, Waukesha, Wisconsin, USA) and a standard 8-channel, receive-only head coil array were used for imaging. A single-shot gradient-recalled echoplanar imaging (EPI) sequence with Sensitivity Encoding (SENSE; [106] was used for fMRI acquisition with the following parameters: FOV/slice thickness/slice gap = 240/2.9/0.5 mm, 41 axial slices per volume, 96 × 96 acquisition matrix, repetition time (TR), echo time (TE) TR/TE= 2000/30 ms, acceleration factor R = 2, flip angle = 90°, sampling bandwidth = 250 kHz. To allow the fMRI signal to reach a steady-state, three EPI volumes (6 s) were excluded from data analysis. For each of three rsfMRI runs, simultaneous physiological

pulse oximetry and respiration waveforms were collected (with 50 Hz sampling, using a photoplethysmograph with an infra-red emitter placed under the pad of the subject's left index finger and a pneumatic respiration belt, respectively). To provide an anatomical reference for the fMRI analysis, a T1-weighted magnetization-prepared rapid gradient-echo (MPRAGE) sequence with SENSE was collected with the following parameters: scan time=4 min 58 sec, FOV=240 mm, axial slices per slab=128, slice thickness=1.2 mm, image matrix=256×256, TR/TE=5/1.9 ms, acceleration factor R=2, flip angle=10°, delay time TD=1400 ms, inversion time TI=725 ms, sampling bandwidth=31.2 kHz. EEG signals were recorded simultaneously with fMRI via a 32-channel MR-compatible EEG system from Brain Products GmbH. The EEG cap consisted of 32 channels, including references, arranged according to the international 10-20 system. One electrode was placed on the subject's back for recording the electrocardiogram (ECG) signal. A Brain Products' SyncBox device was used to synchronize the EEG system clock with the 10 MHz MRI scanner clock. EEG acquisition temporal resolution was 0.2 ms (i.e., 16-bit 5 kS/s sampling), and measurement resolution was 0.1 μV. EEG signals were hardware-filtered throughout acquisition in the frequency band between 0.016 Hz and 250 Hz. Pupil size was recorded in arbitrary units at a sampling rate of 250 samp/sec using an MRC eye tracker system (MRC Systems GmbH, Heidelberg, Germany).

4.3 Data Analysis

Each of the EEG, fMRI, and eye-tracker modalities require specific preprocessing to reduce noise and artifacts, as well as to recover missing data. After applying preprocessing steps separately for the data within each modality, we combined the clean

data from those three modalities. Figure 4-1 shows a summary of data analysis steps as a function of modality.

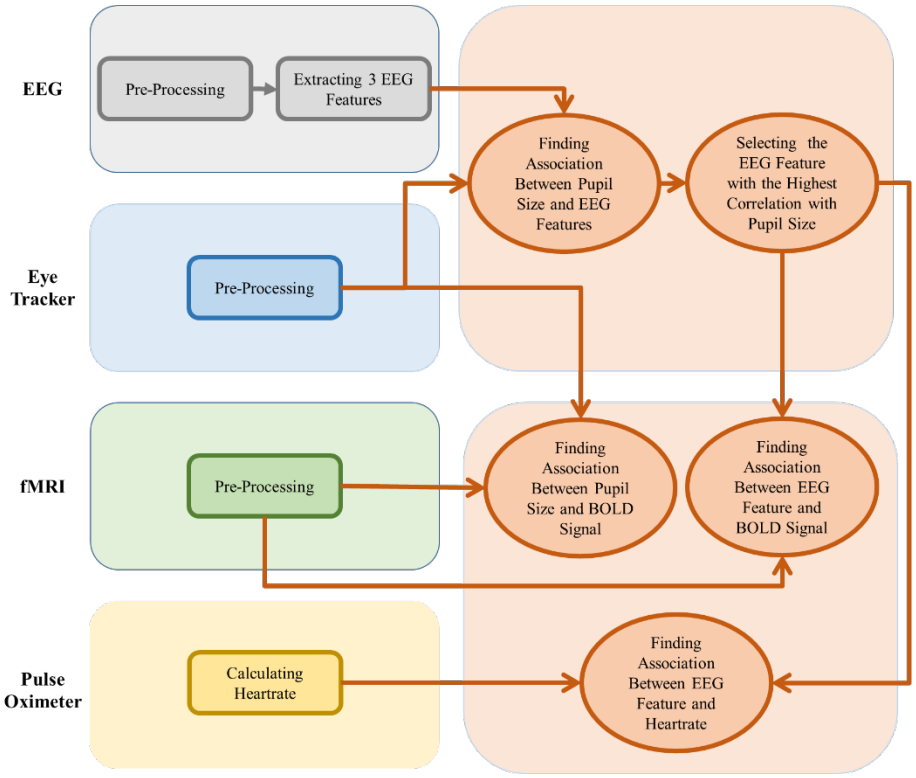

Figure 4-1: The data analysis flowchart.

4.3.1 Preprocessing

As it has discussed in previous chapters EEG is highly sensitive to noise and artifacts. In order to reduce artifacts and preprocess EEG data, we followed the pipeline described in previous chapter and [30].

Pupil size vector includes both missing data due to eye-blinks and noise. In preprocessing the pupil size signal, the "fillmissing" command in MATLAB (MathWorks Inc, Natick, Massachusetts, USA) was used first to interpolate missing numeric data. More specifically, a moving median window with a length of twice the largest gap was

used. Then, a zero Phase Butterworth band-pass filter (0.01–0.1 Hz) was applied to correct for very slow drifts and high-frequency oscillations, as suggested in previously published works [86, 101]. Data from subjects with more than one-third of data missing were excluded, resulting in 21 runs from 10 subjects (the percentage of missing data from each run and participant is shown in Table 4-1).

Table 4-1. Percentages of missing pupil size data

	Percentage of missing data		
Subject Number	**Rest1**	**Rest2**	**Rest3**
Subject 1	0.173	0.188	0.099
Subject 2	0.127	0.23	Not Recorded
Subject 3	0.269	0.133	0.148
Subject 4	0.511	0.168	0.149
Subject 5	0.572	0.551	0.303
Subject 6	Not Recorded	0.177	0.162
Subject 7	0.037	0.081	Not Recorded
Subject 8	0.338	0.271	0.005
Subject 9	0.097	0.831	Fell asleep
Subject 10	0.194	0.137	0.135

Imaging analyses were carried out using the Analysis of Functional NeuroImages software (AFNI, http://afni.nimh.nih.gov/afni/) [107]. The afni_proc.py command was used to preprocess the data using the default parameters. The first three volumes were omitted from the analysis to allow the fMRI signal to reach a steady state. The despike option was adopted to replace outlier time points with interpolation. RETROICOR [108] and respiration volume per time (RVT) correction [109] were applied to remove cardiac-

and respiration-induced noise in the BOLD signal. Slice-timing differences were adjusted by aligning to the first slice, and motion correction was applied by aligning all functional volumes to the first volume. Data were spatially smoothed (6 mm FWHM) and scaled to percent change. Advanced Normalization Tools (ANTs) software [110] was used to apply linear warping to the Talairach template, and the brain resampled to 2 mm^3 voxels (http://stnava.github.io/ANTs/). In order to investigate the effects of physiological noise correction (i.e., RETROICOR and RVT), we repeated the analysis without including these corrections in the preprocessing step.

The heart rate for each individual run and subject was computed using a custom MATLAB script by dividing 60 by the average interval (in seconds) between two R-peaks of the ECG. The values were averaged every 4 seconds.

4.3.2 Postprocessing

After removing the EEG artifact, the following features were extracted using a recent open-source EEG feature extraction software [111] in MATLAB from the EEG data (channels F3, F4, Fz, O1, O2, and Oz) from each subject and each run: (1) power spectral density in the alpha band (alpha power); (2) power spectral density in the beta band (beta power); and (3) the ratio between alpha power and the power in the combined delta and theta bands (alpha ratio; as suggested in literature for the vigilance index during an eyes-closed resting state). We selected these six EEG channels because previous research has shown an association between these channels' features and vigilance, and also because these channels are less vulnerable to artifacts, especially muscle artifacts, than others across the scalp.

PSD was estimated via the periodogram method as follows:

$$\hat{P}(f) = \frac{\Delta t}{N}\left|\sum_{n=0}^{N-1} x_n e^{-j2\pi fn}\right|^2, 0 < f < \frac{1}{2\Delta t}$$

where x_n is the EEG time course, and Δt is the sampling interval. After calculating the PSD in each channel, the power in each frequency band was averaged among the six channels of interest.

The value for each of the three EEG features was averaged every 4 seconds among the selected channels. The average pupil size was calculated every 4 seconds as well, after the aforementioned preprocessing, to generate a pupil size vector for all further analyses. The pupil size vector was used as the vigilance stage index (i.e., larger pupil size indicates a higher vigilance level). The distribution of the pupil size vector and selected EEG features showed a statistically significant deviation from normality ($p < 0.05$) using the Shapiro-Wilk test. Hence, the nonparametric Spearman's rank correlation coefficient ρ was used to measure the correlations between EEG features and pupil size across time within each run and each subject. Furthermore, we used a one-sample t-test on the Fisher z-transformed correlation coefficients to investigate the overall positive EEG feature-pupil size correlation among subjects and to calculate the effect size. In addition, after finding the EEG feature mostly associated with pupil size, we investigated the correlation between that EEG feature and heart rate for each run. Again, we used a one-sample t-test on the Fisher z-transformed correlation coefficients to investigate the overall positive correlation between those features among subjects and computed the effect size. We carried out the same analysis with the features extracted from all channels (instead of only six channels) to confirm the reliability of the EEG feature we selected as the vigilance index. Next, pupil size and EEG features were applied to fMRI data analysis as separate

regressors. Each of these regressors was convolved with a hemodynamic response function (HRF) and downsampled to 0.5 Hz (to match the TR of 2 s) if needed.

4.4 Results

Correlations between EEG features from channels F3, F4, Fz, O1, O2, and Oz (i.e., alpha power, beta power, and the alpha ratio) and pupil size are summarized in Figure 4-2. We repeated these analyses by extracting EEG features from all channels, and the results are shown in Figure 4-3. The statistical details of correlations between pupil size and EEG features, as well as one sample t-test and effect size on the Fisher z-transformed correlation coefficient results, are shown in Table 4-2.

Table 4-2. The details of correlations between pupil size and EEG features.

		Average of Correlation Coefficient	STD of Correlation Coefficient	One-Pair T-Test on r to z transformed		Cohen's Effect Size	
				df	p-value	t-stat	
6 Selected Channels	Alpha Power	0.231	0.115	9	0.001	4.739	1.499
	Beta Power	0.306	0.107	9	2.90E-06	10.254	3.241
	Alpha ratio	-0.036	0.109	9	0.338	-1.01	-0.319
All 31 Channels	Alpha Power	0.233	0.155	9	0.001	4.627	1.463
	Beta Power	0.306	0.091	9	3.80E-06	9.922	3.136
	Alpha ratio	-0.043	0.117	9	0.283	-1.143	-0.361

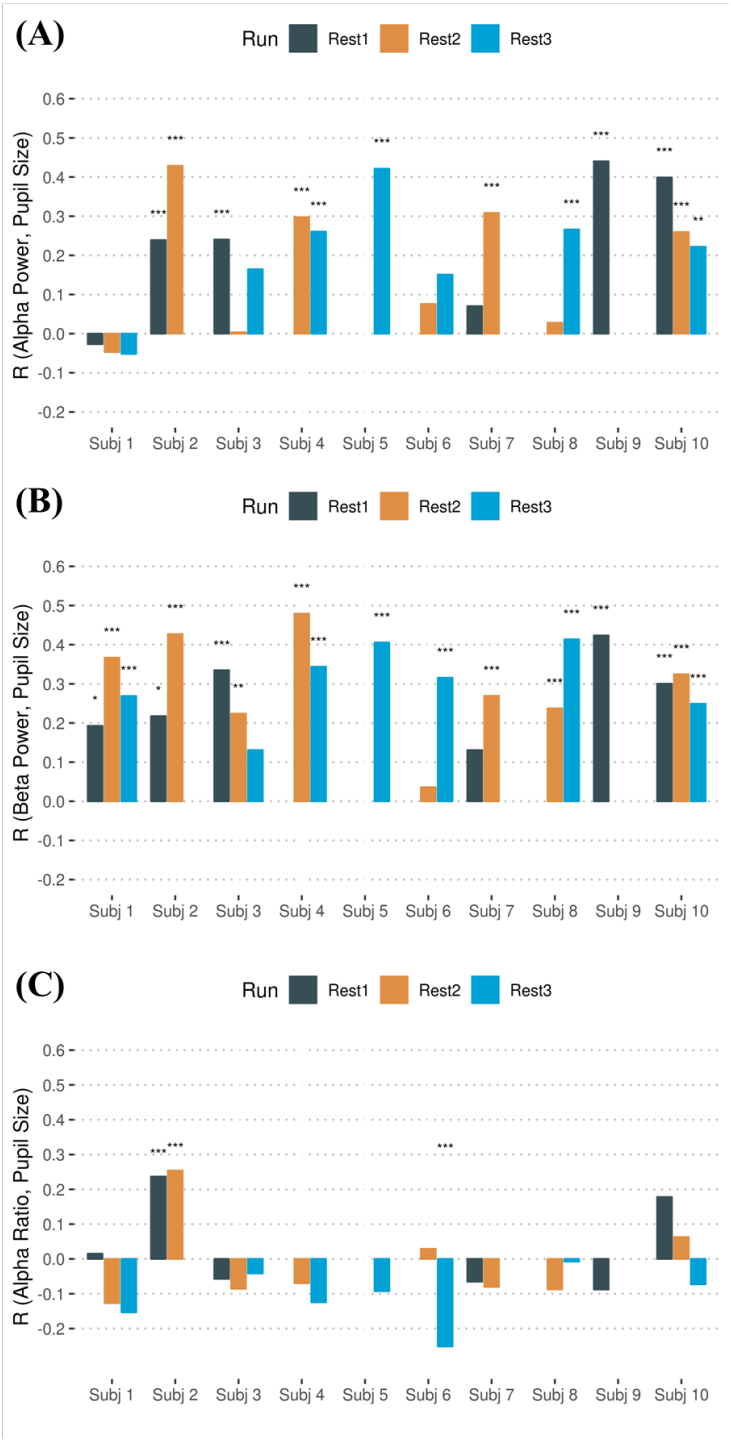

Figure 4-2: Association between following EEG features from frontal (i.e., (F3, F4, and Fz) and occipital (O1, O2, and Oz)) electrodes: (A) Alpha power; (B) Beta power; (C) Alpha ration and the pupil size.

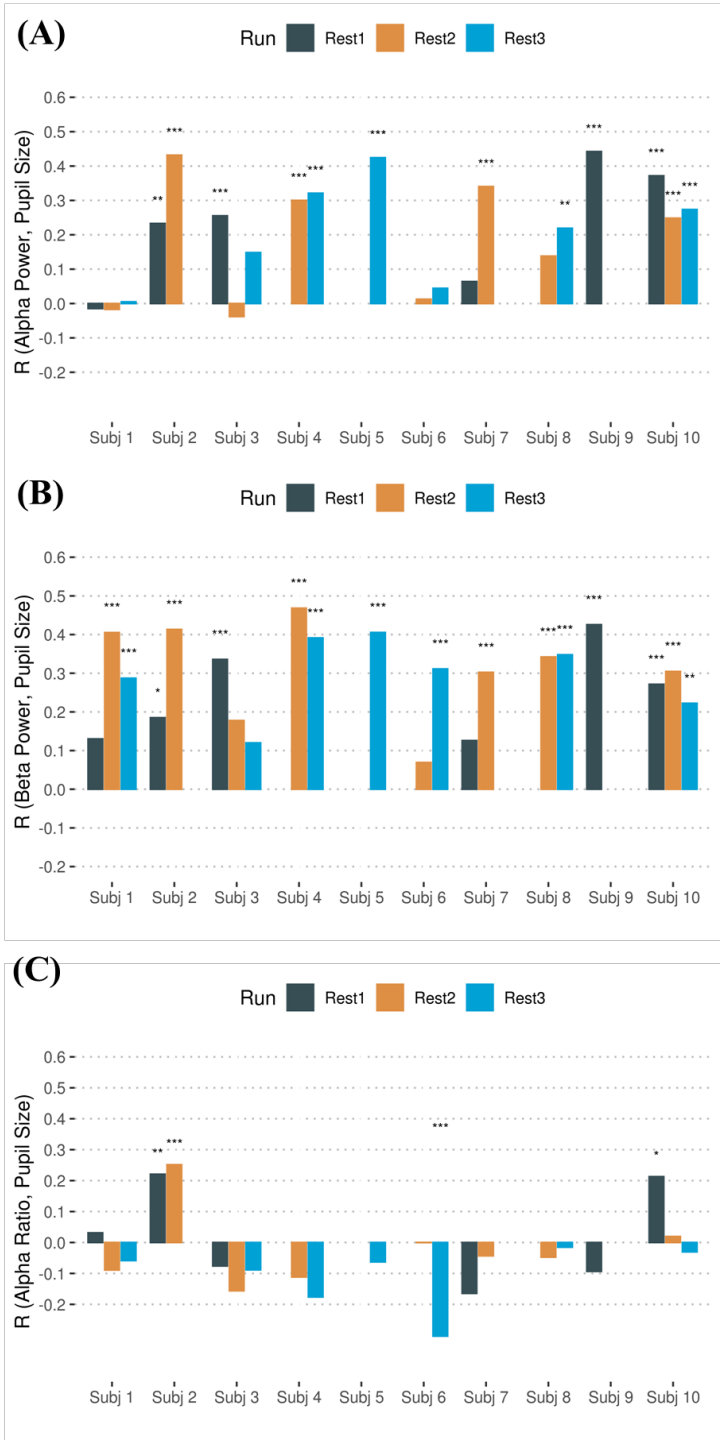

Figure 4-3: Association between the following average EEG features among all channels: (A) Alpha power; (B) Beta power; (C) Alpha ration, and pupil size.

The correlation coefficients in Table 4-2 show an overall positive correlation between pupil size vector and both alpha and beta power, which indicates that higher alpha/beta powers represent larger pupil size (and vigilance level). We further compared the Fisher z-transformed correlation coefficients between alpha power and pupil size and between beta power and pupil size from the selected six EEG channels. The results are as follow: $t(18) = -2.162, p = 0.058$. The difference between these correlations shows a trend to a significant difference. Also, the results presented in Figure 4-2 show the correlation between pupil size and beta power was insignificant for 3 of 21 runs; however, 9 out of 21 runs were not significant for alpha power association with pupil size. Therefore, we used frontal and occipital beta power (FOBP; as the vigilance level index) as a regressor for the fMRI analysis. Figure 4-4 depicts the correlation map between BOLD signal with correction for physiological noise and FOBP. The analysis was performed for each voxel, and the statistical map was thresholded with voxel-wise $p < 0.005$ and cluster-size corrected at $p < 0.05$. The cluster-size threshold was evaluated with AFNI's 3dClustSim using an improved spatial autocorrelation function (ACF; [112]); a minimum cluster size of 146 voxels was required to have a corrected $p \leq 0.05$ while using 2-sided third nearest neighbor clustering (NN3). Table 4-3 illustrates that higher values of beta power were associated with a greater BOLD signal in the precentral gyrus, postcentral gyrus, and insular cortex, as well as in the temporal gyrus and inferior parietal lobule. The results related to the correlation map of the BOLD signal without correction for physiological noise and FOBP are shown in Figure 4-5 and Table 4-4.

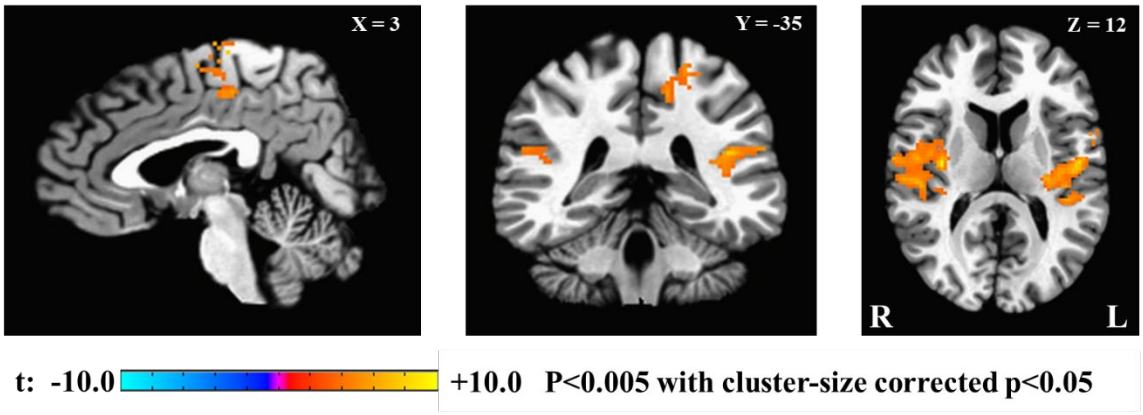

Figure 4-4: Power spectral density in the frontal and occipital beta power (FOBP) correlation Map.

Table 4-3. Brain regions correlated to power spectral density in frontal and occipital beta power (FOBP).

Cluster	Peak coordinate (Talairach)				
	x	y	z	t-score	Cluster size (# voxels)
Insula (R), Claustrum (R), Superior temporal gyrus (R), pretcentral gyrus (R) , transverse temporal gyrus (R), , postcentral gyrus (R)	33	-13	12	9.416	1052
Insula (L), superior temporal gyrus (L), Claustrum (L), precentral gyrus (L), postcentral gyrus (L), inferior parietal lobule (L)	-51	-9	18	9.719	792
Medial frontal gyrus (R), paracentral lobule (R), paracentral lobule (L)	3	-23	64	8.004	191
Paracentral gyrus (L), postcentral gyrus (L), inferior parietal lobule (L)	-23	-39	54	6.924	155

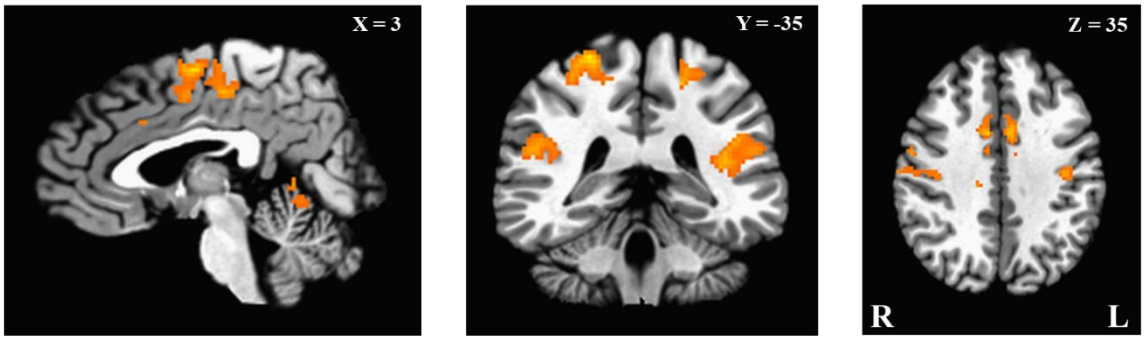

Figure 4-5: Power spectral density in the frontal and occipital beta power (FOBP) correlation Map without physiological noise correction.

Table 4-4. Brain regions correlated to power spectral density in the beta band (channels F3, F4, Fz, O1, O2, and Oz) without physiological noise correction.

Cluster	Peak coordinate (Talairach)				Cluster size (# voxels)
	x	y	z	t-score	
Insula (R), Claustrum (R), Superior temporal gyrus (R), pretcentral gyrus (R) , transverse temporal gyrus (R), postcentral gyrus (R), inferior parietal lobule (R)	57	-11	14	11.799	1582
Insula (L), superior temporal gyrus (L), Claustrum (L), precentral gyrus (L), postcentral gyrus (L), inferior parietal lobule (L)	-49	-13	16	11.149	1172
Medial frontal gyrus (R), paracentral lobule (R), paracentral lobule (L), Cingulate Gyrus (R), Cingulate Gyrus (L),	3	-7	56	8.221	764
Paracentral gyrus (L), postcentral gyrus (L)	-21	-39	56	7.261	229
Precentral gyrus (L), postcentral gyrus (L)	-39	-17	40	7.888	227
Postcentral gyrus (R)	23	-35	62	8.990	211
Culmen (R), Declive (R), Culmen (L)	7	-57	-8	8.984	168

Figure 4-6 illustrates correlations between heart rate and FOBP (results of one-sample t-test on the Fisher z-transformed correlation coefficients: *t(9)= 4.625*, *p=0.001*, *d=1.462).* Figure 4-7 illustrates the correlation between heart rate and beta power including all EEG channels (*t(9)= 4.797*, *p= 9.8e-04*, *d= 1.517*).

Finally, Figure 4-8 shows the correlation maps between the BOLD signal with correction for physiological noise and pupil size. Table 4-5 shows the details of the brain regions associated with that regressor, with larger pupil size, linked to lower fronto-occipital BOLD signal. The results for the same analysis without correction for physiological noise are presented in Figure 4-9 and Table 4-6.

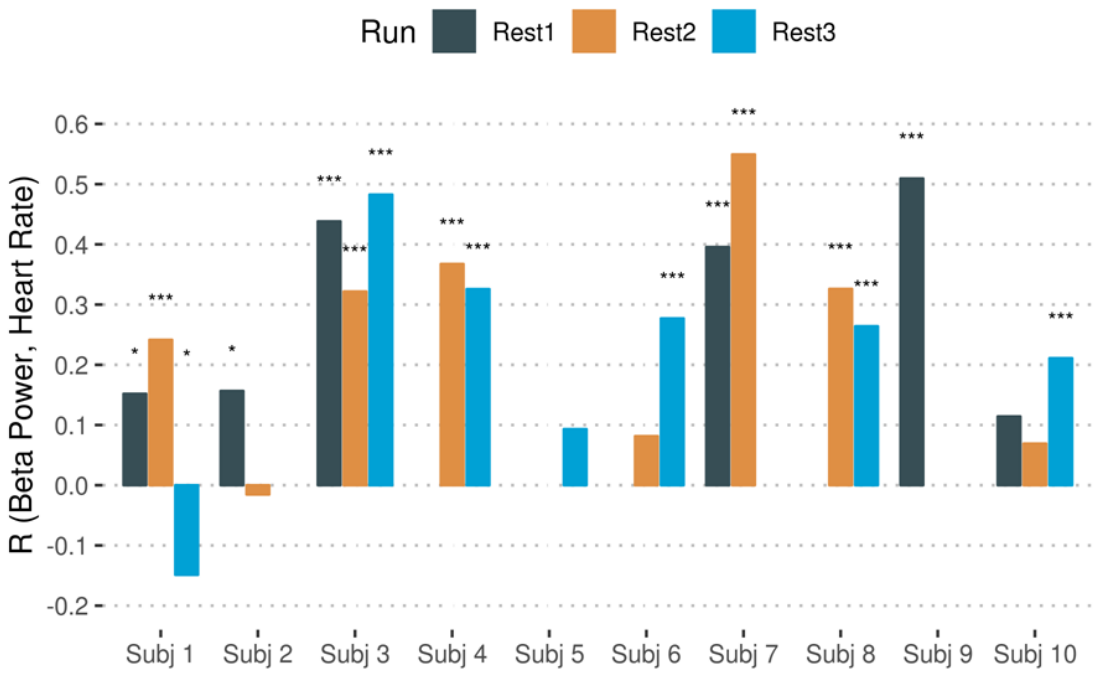

Figure 4-6: Association between frontal and occipital beta power (FOBP) and heart rate.

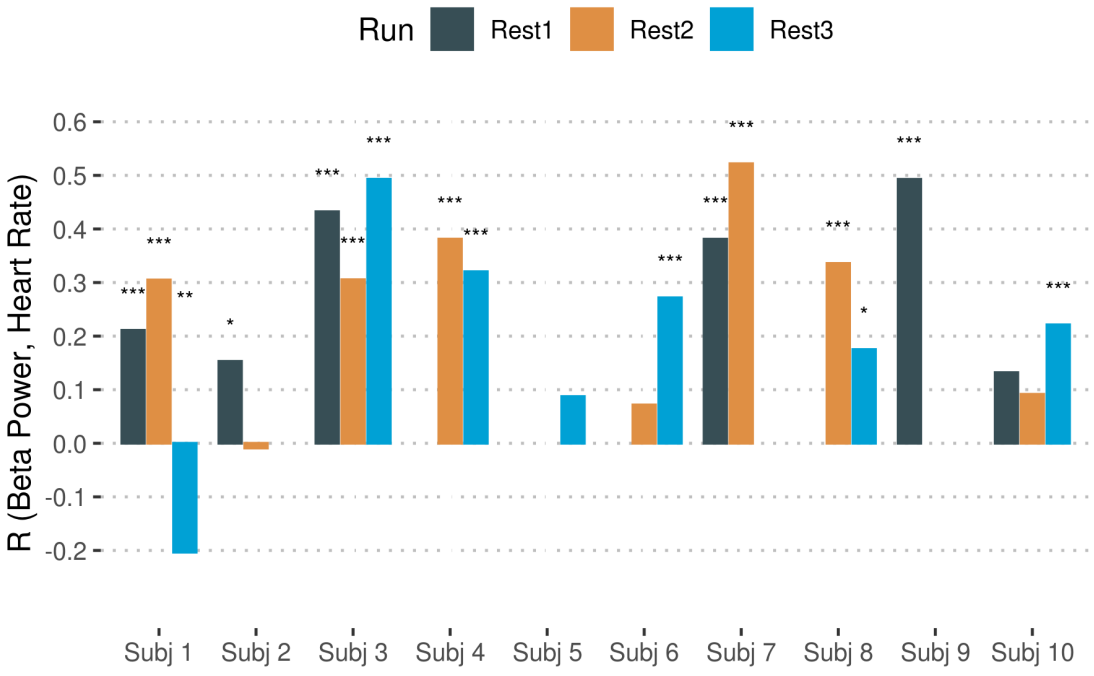

Figure 4-7: Association Between EEG Power in Beta Band and heart rate.

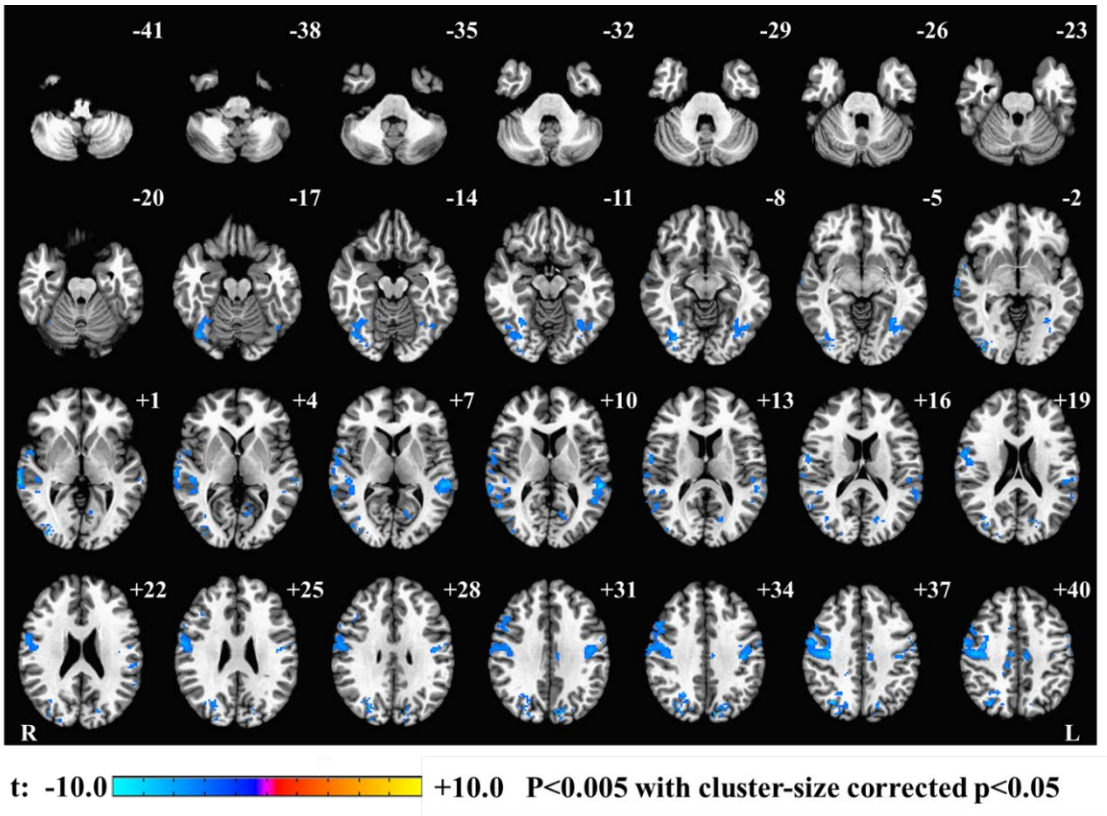

Figure 4-8: Pupil size
correlation map achieved by using pupil size as a regressor in fMRI GLM analysis.

Table 4-5. Brain regions correlated to pupil size.

Cluster	Peak coordinate (Talairach)				Cluster size (# voxels)
	x	y	z	t-score	
Middle frontal gyrus (R), precentral gyrus (R) , postcentral gyrus (R), middle cingulate gyrus, paracentral gyrus, medial frontal gyrus	25	-27	56	-12.903	3494
Declive (R), fusiform gyrus (R), inferior occipital gyrus (R), middle occipital gyrus (R), precuneus (R), lingual gyrus (R)	35	-85	-2	-10.625	684
Superior temporal gyrus (L), postcentral gyrus (L)	-53	-35	10	-13.792	299
Precentral gyrus (L)	-43	-13	52	-9.921	262
Parahippocampal gyrus (L), fusiform gyrus (L), inferior occipital gyrus (L), middle occipital gyrus (L), Declive (L)	-33	-55	-4	-7.54	205
Cuneus (L), precuneus (L), lingual gyrus (l)	-9	-79	34	-7.082	185

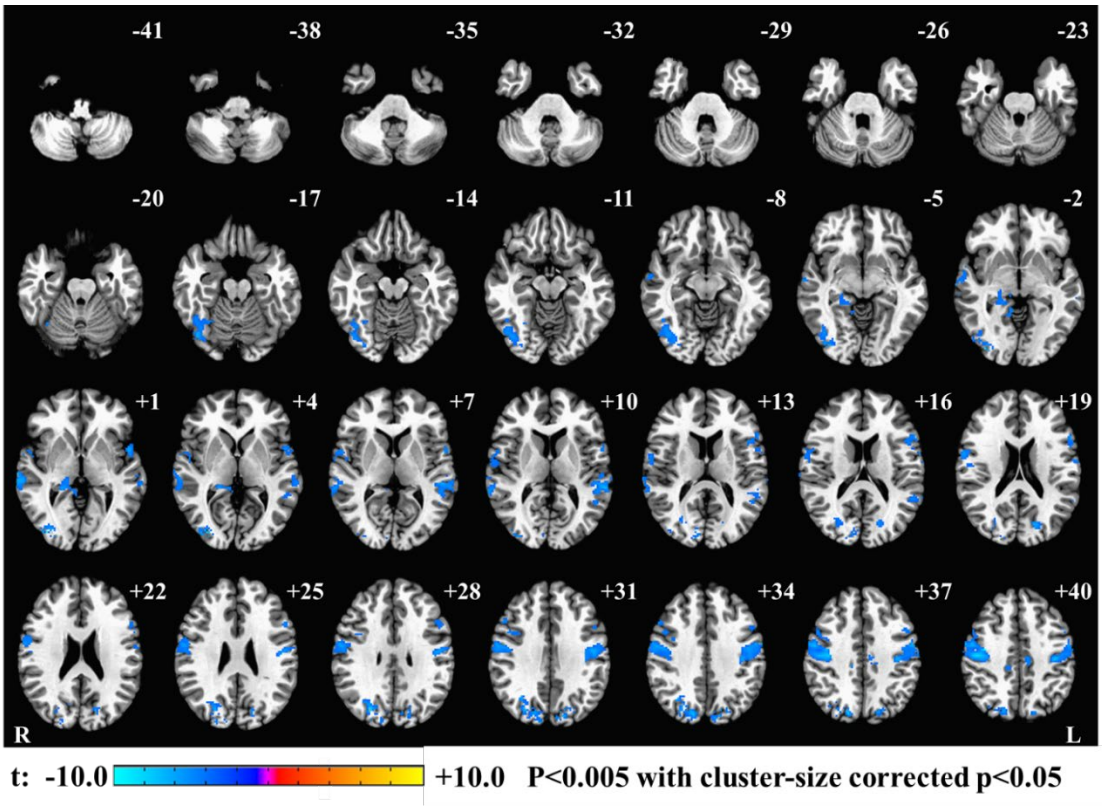

Figure 4-9: Pupil size correlation map without physiological noise correction, achieved by using pupil size as a regressor in fMRI GLM analysis.

Table 4-6. Brain regions correlated to pupil size without physiological noise correction.

Cluster	Peak coordinate (Talairach)				Cluster size (# voxels)
	x	y	z	t-score	
Middle temporal gyrus (R), Superior temporal gyrus (R), paracentral gyrus (R) , paracentral gyrus (L), postcentral gyrus (R), middle cingulate gyrus (R)	65	-31	0	-9.969	3789
Precentral gyrus (L), postcentral gyrus (L)	-43	-15	50	-9.940	672
Declive (R), fusiform gyrus (R), inferior occipital gyrus (R), middle occipital gyrus (R), lingual gyrus (R	35	-81	2	-10.214	520
Cuneus (R), precuneus (R), middle occipital gyrus (R),	25	-71	28	-7.868	441
Superior temporal gyrus (L), transverse temporal gyrus (L)	-57	-35	10	-7.025	290
Superior temporal gyrus (L), inferior frontal gyrus (L), precentral gyrus (L)	-49	5	2	-5.942	247
Cuneus (L), precuneus (L)	-15	-73	18	-7.082	183
Parahippocampal gyrus (R), culmen (R)	19	-35	2	-5.867	162

4.5 Discussion

This study aimed to determine whether EEG features could be used as objective markers of vigilance in healthy human subjects during eyes-open rsfMRI experiments. The investigation revealed three main findings: First, frontal (F3, F4, and Fz) and occipital (O1, O2, and Oz) beta power (i.e., FOBP) showed the highest correlation with pupil size; Second, FOBP correlated with several brain regions that have been implicated in modulating vigilance; Third, FOBP was also positively correlated with heart rate.

Taken together, these findings support the conclusion that FOBP is an objective and robust biomarker of vigilance in healthy human subjects.

As shown in Figure 4-2, there is not a significant correlation between pupil size and FOBP in 3 out of 21 runs. An earlier simultaneous EEG- fMRI study [113], suggested that the alpha rhythm signal was associated with "inattention" during rest, while beta rhythms were posited to index spontaneous cognitive operations during conscious rest. For the rest of our analysis, we considered FOBP as the vigilance index during our eyes-open resting state.

Although we tested the correlation between the ratio of the PSD in the alpha band, the power in the combined delta and theta band (the most common measure of vigilance during eyes-closed resting state), and pupil size, show an insignificant association. This conclusion could indicate the difference between EEG vigilance measures in eyes-open and eyes-closed conditions. [96] found a significant correlation between the mean alpha level across all channels and skin conductance levels as an index for vigilance across the eyes-closed condition. However, no correlations between skin conductance levels and alpha power were reported in the study during their eyes-open condition, so it is possible that the alpha ratio-arousal association only holds for eyes-closed data. A very recent simultaneous EEG-fMRI study [79] used the ratio of power in the alpha band over the power in the delta and theta bands as the vigilance index for both eyes-open and eyes-closed conditions. Their results suggested a significant difference between the vigilance index BOLD correlation map in the thalamus and DMN among eyes-open and eyes-closed conditions [79].

After capturing EEG feature with the highest correlation with pupil size, this feature (e.g., EEG power in beta band) served as a regressor for fMRI analysis, as illustrated in Figure 4-3. The correlation map for FOBP shows positive correlations with several brain regions, including the bilateral insula, inferior parietal lobule, and supplementary motor area. Interestingly, these brain regions have been reported in all previous studies investigating the correlation maps of EEG vigilance indices during eyes-closed rsfMRI [5, 79, 89]. Further, these brain regions are all parts of the anti-correlated network (ACN) [114, 115], which has shown anti-correlated activation with the DMN both during the rsfMRI and task-based analysis.

A previous study [78] showed that using respiration volume per time (RVT) and retrospective correction of physiological motion effects (RETROICOR) for physiological correction has fewer effects on the EEG (alpha power) correlation map during eyes-open compared to eyes-closed rsfMRI. To investigate the effects of physiological noise correction, we showed the FOBP and pupil correlation maps without including physiological noise correction. The results presented in Table 4-3 and Table 4-4 show that the same brain regions were found correlated with FOBP regardless of physiological noise correction. It is worth noting, however, that without using physiological noise correction, the BOLD signal in cerebellum (e.g., declive and culmen) is correlated with FOBP. This is in line with the results presented in [78], which found RETRICOR and RVT correction has a minimum effect on an EEG correlation map with a BOLD signal during eyes-open rsfMRI. BOLD activity (after physiological noise correction) from several brain regions that correlated with pupil size repeats when no noise correction is

used. This indicates the low effects of physiological noise correction for eyes-open rsfMRI.

Furthermore, to validate our findings with fMRI, we examined the correlation between the selected EEG vigilance features and heart rate. As previous studies (for example [5]) have shown higher vigilance was associated with a higher heart rate. Figure 4 represents such a positive correlation. In an earlier study, we found a positive correlation between pupil size and beta power, and that feature had a positive correlation with heart rate. Therefore, heart rates increase with a higher vigilance level.

Additionally, to compute the EEG features from the aforementioned six channels, we repeated the analysis with the extraction of EEG features from all 31 channels. As Figure 4-3 and Figure 4-7 show, the association between pupil size and both alpha and beta powers, as well as the correlation between beta power and heart rate, are still significantly higher than zero when using all 31 EEG channels. However, the results from six and all 31 channels are slightly varied for EEG features related to the beta band as compared to the alpha band (e.g., five runs out of 21 total do not show significant correlation between pupil size and beta power using 31 channels; compared to three runs for six channels), and that could be due to residual muscle and imaging artifacts in the beta band, especially at the edge electrodes (e.g., TP9 and TP10). We specifically selected those six channels because they have been used in previous studies for investigating the vigilance level [5, 88] and because they are less vulnerable to noise and artifacts.

Finally, pupil size served as a regressor for fMRI. In contrast with previous studies that found a positive correlation between pupil size and DMN [101] and the thalamus, caudate nucleus and cerebellum [86], our results revealed widespread negative

correlations between pupil size and the BOLD signal within visual and sensorimotor cortices as well as within the middle cingulate gyrus, precuneus, and cuneus. It should be noted that in Schneider et al. (2016) study benefitted from a larger sample size than the one used in this study. This could be a contributing factor that our results didn't identify similar correlated brain regions.

Our discovered brain regions have appeared in previous studies [5, 89]. Physiological noise correction was not conducted in [86], and when we did not use such correction in our analysis, we found exactly the same brain regions anti-correlated with pupil size as in [89].

4.6 Conclusion

Simultaneous EEG-fMRI-eye-tracker experiments have been suggested in an effort to determine, verify, and measure participant arousal/vigilance level during rsfMRI, especially with the use of eye tracker system as most widely accepted technique to assess subject's vigilance level. However, such an experimental setup requires specific, and often costly, hardware, and software. More specifically, the eye-tracker system makes the experimental setup difficult and less widely utilized. Furthermore, the analysis of data within each of these modalities requires a skilled workforce. In this study, we designed and conducted the first multimodal EEG-rsfMRI-eye-tracker experiment in human participants **(**to the best of our knowledge**)**. Our results revealed an association between frontal and occipital beta power and degree of vigilance during an eyes-open resting state. This association could be more easily determined during simultaneous EEG-fMRI and even provide a real-time test of subject vigilance in resting-state fMRI. We validated the

results using simultaneously-recorded heart rate and fMRI. Notably, independently-verified heart rate changes can also provide an easy-to-determine measure of vigilance during rsfMRI.

Chapter 5: Conclusion and Future Work

5.1 Conclusion

New tools to improve data quality are necessary to accommodate the increase in simultaneous EEG-fMRI studies for investigating human brain functionality. The work presented in this dissertation focused on two critical aspects of simultaneous EEG-fMRI studies.

The first was the presentation of MRI-environment artifacts in EEG data acquired during fMRI acquisition. When compared with data recorded outside the MRI, the EEG data are contaminated with additional extraneous artifacts. Reducing these artifacts is time-consuming and requires specific skills and expertise. This issue becomes more problematic for large studies (e.g., Tulsa-1000 study). Reducing such contamination from EEG data requires a fully automated artifact correction approach, as proposed herein. The algorithm combines the template correction approaches (i.e., OBS, AAS), along with ICA, to remove both MRI-environment artifacts and physiological artifacts (e.g., ocular and muscle artifacts). The automated pipeline for EEG artifact reduction recorded during fMRI (APPEAR) was validated using resting-state and task-based EEG-fMRI data, and then compared with manually-corrected EEG data. Results confirm slight to no difference between automated- and manually-corrected EEG data. Hence, APPEAR is proposed as

a standard pipeline for reducing EEG artifacts recorded simultaneously with fMRI, especially for large simultaneously EEG-fMRI studies. An automated method will improve data preparation efficiency and remove bias from human/operator factors.

An additional technique was introduced to better control resting-state EEG-fMRI study experimentations. The technique utilizes an eye tracker to monitor eye state (e.g., open/closed) and pupil size when eyes are open. During eyes-open rsfMRI, subjects are assumed awake and vigilant, although this assumption must be confirmed during scans. Lack of such information may cause variability in the BOLD signal for different brain regions and functional connectivity. The proposed use of an eye tracker indicates subject's vigilance by measuring the subject's pupil size. Although simultaneous EEG-fMRI techniques are widely used for studying the human brain, simultaneous eye tracker-fMRI techniques are not. This study examined an EEG feature with pupil dimension (i.e., FOBP) and found that the association among feature, heart-rate, and BOLD fMRI data is a good measure of subject vigilance during rsfMRI. This information alone can be used for future EEG-fMRI studies, removing the need to use an eye tracker device.

5.2 Future Works

Several aspects of the proposed methods could be considered for ensuring improvement, including the following advancements.

1- QRS cycle detection for generating an accurate BCG artifact could be enhanced, as it has important effects on the proposed pipeline. Furthermore, the computation speed of the algorithm must be improved when intended to use in real-time applications.

2- Although an eye-tracker was used as an indirect measure of vigilance during eyes-open resting state, there is no guarantee that participants will keep their eyes open during the entire scan time. Therefore, it will be necessary to test if FOBP could serve as an appropriate EEG vigilance measure during eyes-closed resting state. It is important to note that an eye-tracker device is not a helpful tool for eyes-closed scans. Instead, skin conductivity and heart-rate parameters are suggested as possible indicators.

References

[1] M. E. Raichle, "Functional brain imaging and human brain function," *Journal of Neuroscience,* vol. 23, no. 10, pp. 3959-3962, 2003.

[2] R. Caton, "Electrical currents of the brain," *The Journal of Nervous and Mental Disease,* vol. 2, no. 4, p. 610, 1875.

[3] H. Berger, "Über das elektrenkephalogramm des menschen," *European archives of psychiatry and clinical neuroscience,* vol. 87, no. 1, pp. 527-570, 1929.

[4] E. D. Adrian and B. H. Matthews, "The Berger rhythm: potential changes from the occipital lobes in man," *Brain,* vol. 57, no. 4, pp. 355-385, 1934.

[5] S. Olbrich *et al.*, "EEG-vigilance and BOLD effect during simultaneous EEG/fMRI measurement," *Neuroimage,* vol. 45, no. 2, pp. 319-332, 2009.

[6] W. Klimesch, "EEG alpha and theta oscillations reflect cognitive and memory performance: a review and analysis," *Brain research reviews,* vol. 29, no. 2-3, pp. 169-195, 1999.

[7] F. Ferrarelli, R. Kaskie, S. Laxminarayan, S. Ramakrishnan, J. Reifman, and A. Germain, "An increase in sleep slow waves predicts better working memory performance in healthy individuals," *NeuroImage,* vol. 191, pp. 1-9, 2019.

[8] D. L. Schacter, "EEG theta waves and psychological phenomena: A review and analysis," *Biological psychology,* vol. 5, no. 1, pp. 47-82, 1977.

[9] B. Burle, L. Spieser, C. Roger, L. Casini, T. Hasbroucq, and F. Vidal, "Spatial and temporal resolutions of EEG: Is it really black and white? A scalp current density view," *International Journal of Psychophysiology,* vol. 97, no. 3, pp. 210-220, 2015.

[10] F. A. Rahman, M. F. Othman, and N. A. Shaharuddin, "A review on the current state of artifact removal methods for electroencephalogram signals," in *2015 10th Asian Control Conference (ASCC)*, 2015, pp. 1-6: IEEE.

[11] O. G. Lins, T. W. Picton, P. Berg, and M. Scherg, "Ocular artifacts in EEG and event-related potentials I: Scalp topography," *Brain topography,* vol. 6, no. 1, pp. 51-63, 1993.

[12] B. W. McMenamin *et al.*, "Validation of ICA-based myogenic artifact correction for scalp and source-localized EEG," *Neuroimage,* vol. 49, no. 3, pp. 2416-2432, 2010.

[13] J. W. Britton *et al.*, *Electroencephalography (EEG): An introductory text and atlas of normal and abnormal findings in adults, children, and infants*. American Epilepsy Society, Chicago, 2016.

[14] S. Hidalgo-Tobon, "Theory of gradient coil design methods for magnetic resonance imaging," *Concepts in Magnetic Resonance Part A,* vol. 36, no. 4, pp. 223-242, 2010.

[15] S. A. Huettel, A. W. Song, and G. McCarthy, *Functional magnetic resonance imaging*. Sinauer Associates Sunderland, MA, 2004.

[16] C. Mulert and L. Lemieux, *EEG-fMRI: physiological basis, technique, and applications*. Springer Science & Business Media, 2009.

[17] L. Lemieux, P. Allen, K. Krakow, M. Symms, and D. Fish, "Methodological issues in EEG-correlated functional MRI experiments," *IJBEM,* vol. 1, no. 1, pp. 87-95, 1999.

[18] C. Mulert, "Simultaneous EEG and fMRI: towards the characterization of structure and dynamics of brain networks," *Dialogues in clinical neuroscience,* vol. 15, no. 3, p. 381, 2013.

[19] K. Mullinger, S. Debener, R. Coxon, and R. Bowtell, "Effects of simultaneous EEG recording on MRI data quality at 1.5, 3 and 7 tesla," *International Journal of Psychophysiology,* vol. 67, no. 3, pp. 178-188, 2008.

[20] D. Carmichael, "Image quality issues," in *EEG-fMRI*: Springer, 2009, pp. 173-199.

[21] P. Ritter, R. Becker, F. Freyer, and A. Villringer, "EEG quality: the image acquisition artefact," in *EEG-fMRI*: Springer, 2009, pp. 153-171.

[22] P. J. Allen, O. Josephs, and R. Turner, "A method for removing imaging artifact from continuous EEG recorded during functional MRI," *Neuroimage,* vol. 12, no. 2, pp. 230-239, 2000.

[23] R. K. Niazy, C. F. Beckmann, G. D. Iannetti, J. M. Brady, and S. M. Smith, "Removal of FMRI environment artifacts from EEG data using optimal basis sets," *Neuroimage,* vol. 28, no. 3, pp. 720-737, 2005.

[24] H. Laufs, "A personalized history of EEG–fMRI integration," *Neuroimage,* vol. 62, no. 2, pp. 1056-1067, 2012.

[25] S. M. Wierda, H. van Rijn, N. A. Taatgen, and S. Martens, "Pupil dilation deconvolution reveals the dynamics of attention at high temporal resolution," *Proceedings of the National Academy of Sciences,* vol. 109, no. 22, pp. 8456-8460, 2012.

[26] D. Mantini, M. G. Perrucci, S. Cugini, A. Ferretti, G. L. Romani, and C. Del Gratta, "Complete artifact removal for EEG recorded during continuous fMRI using independent component analysis," *Neuroimage,* vol. 34, no. 2, pp. 598-607, 2007.

[27] X. Wu, T. Wu, Z. Zhan, L. Yao, and X. Wen, "A real-time method to reduce ballistocardiogram artifacts from EEG during fMRI based on optimal basis sets (OBS)," *Computer methods and programs in biomedicine,* vol. 127, pp. 114-125, 2016.

[28] P. J. Allen, G. Polizzi, K. Krakow, D. R. Fish, and L. Lemieux, "Identification of EEG events in the MR scanner: the problem of pulse artifact and a method for its subtraction," *Neuroimage,* vol. 8, no. 3, pp. 229-239, 1998.

[29] A. Mayeli, V. Zotev, H. Refai, and J. Bodurka, "An automatic ICA-based method for removing artifacts from EEG data acquired during fMRI in real time," in *2015 41st Annual Northeast Biomedical Engineering Conference (NEBEC)*, 2015, pp. 1-2: IEEE.

[30] A. Mayeli, V. Zotev, H. Refai, and J. Bodurka, "Real-time EEG artifact correction during fMRI using ICA," *Journal of neuroscience methods,* vol. 274, pp. 27-37, 2016.

[31] V. Zotev *et al.*, "Correlation between amygdala BOLD activity and frontal EEG asymmetry during real-time fMRI neurofeedback training in patients with depression," *NeuroImage: Clinical,* vol. 11, pp. 224-238, 2016.

[32] S. Debener, C. Kranczioch, and I. Gutberlet, "EEG quality: origin and reduction of the EEG cardiac-related artefact," in *EEG-fMRI*: Springer, 2009, pp. 135-151.

[33] G. Bonmassar *et al.*, "Motion and ballistocardiogram artifact removal for interleaved recording of EEG and EPs during MRI," *Neuroimage,* vol. 16, no. 4, pp. 1127-1141, 2002.

[34] W. J. R. Dunseath and T. A. Alden, "Apparatus and method for acquiring a signal," ed: Google Patents, 2010.

[35] Q. Luo, X. Huang, and G. H. Glover, "Ballistocardiogram artifact removal with a reference layer and standard EEG cap," *Journal of neuroscience methods,* vol. 233, pp. 137-149, 2014.

[36] R. A. Masterton, D. F. Abbott, S. W. Fleming, and G. D. Jackson, "Measurement and reduction of motion and ballistocardiogram artefacts from simultaneous EEG and fMRI recordings," *Neuroimage,* vol. 37, no. 1, pp. 202-211, 2007.

[37] J. N. van der Meer *et al.*, "Carbon-wire loop based artifact correction outperforms post-processing EEG/fMRI corrections—A validation of a real-time simultaneous EEG/fMRI correction method," *Neuroimage,* vol. 125, pp. 880-894, 2016.

[38] M. E. Chowdhury *et al.*, "Reference Layer Artefact Subtraction (RLAS): Electromagnetic Simulations," *IEEE Access,* vol. 7, pp. 17882-17895, 2019.

[39] A. J. Daniel, J. A. Smith, G. S. Spencer, J. Jorge, R. Bowtell, and K. J. Mullinger, "Exploring the relative efficacy of motion artefact correction techniques for EEG data acquired during simultaneous fMRI," *Human brain mapping,* vol. 40, no. 2, pp. 578-596, 2019.

[40] J. Jorge, F. Grouiller, R. Gruetter, W. Van Der Zwaag, and P. Figueiredo, "Towards high-quality simultaneous EEG-fMRI at 7 T: detection and reduction of EEG artifacts due to head motion," *Neuroimage,* vol. 120, pp. 143-153, 2015.

[41] V. Zotev, M. Misaki, R. Phillips, C. K. Wong, and J. Bodurka, "Real-time fMRI neurofeedback of the mediodorsal and anterior thalamus enhances correlation between thalamic BOLD activity and alpha EEG rhythm," *Human brain mapping,* vol. 39, no. 2, pp. 1024-1042, 2018.

[42] V. Zotev, R. Phillips, H. Yuan, M. Misaki, and J. Bodurka, "Self-regulation of human brain activity using simultaneous real-time fMRI and EEG neurofeedback," *NeuroImage,* vol. 85, pp. 985-995, 2014.

[43] A. Delorme, S. Makeig, and T. Sejnowski, "Automatic artifact rejection for EEG data using high-order statistics and independent component analysis," in *Proceedings of the third international ICA conference*, 2001, pp. 9-12.

[44] P. LeVan, E. Urrestarazu, and J. Gotman, "A system for automatic artifact removal in ictal scalp EEG based on independent component analysis and Bayesian classification," *Clinical Neurophysiology,* vol. 117, no. 4, pp. 912-927, 2006.

[45] G. Srivastava, S. Crottaz-Herbette, K. Lau, G. Glover, and V. Menon, "ICA-based procedures for removing ballistocardiogram artifacts from EEG data acquired in the MRI scanner," *Neuroimage,* vol. 24, no. 1, pp. 50-60, 2005.

[46] R. Abreu *et al.*, "Ballistocardiogram artifact correction taking into account physiological signal preservation in simultaneous EEG-fMRI," *Neuroimage,* vol. 135, pp. 45-63, 2016.

[47] S. Debener, K. J. Mullinger, R. K. Niazy, and R. W. Bowtell, "Properties of the ballistocardiogram artefact as revealed by EEG recordings at 1.5, 3 and 7 T static magnetic field strength," *International Journal of Psychophysiology,* vol. 67, no. 3, pp. 189-199, 2008.

[48] A. Delorme and S. Makeig, "EEGLAB: an open source toolbox for analysis of single-trial EEG dynamics including independent component analysis," *Journal of neuroscience methods,* vol. 134, no. 1, pp. 9-21, 2004.

[49] C.-K. Wong, Q. Luo, V. Zotev, R. Phillips, K. W. C. Chan, and J. Bodurka, "Automatic cardiac cycle determination directly from EEG-fMRI data by multi-scale peak detection method," *Journal of neuroscience methods,* vol. 304, pp. 168-184, 2018.

[50] J. Jorge, C. Bouloc, L. Bréchet, C. M. Michel, and R. Gruetter, "Investigating the variability of cardiac pulse artifacts across heartbeats in simultaneous EEG-fMRI recordings: A 7T study," *NeuroImage,* vol. 191, pp. 21-35, 2019.

[51] F. Ghaderi, K. Nazarpour, J. G. McWhirter, and S. Sanei, "Removal of ballistocardiogram artifacts exploiting second order cyclostationarity," in *2010 IEEE International Workshop on Machine Learning for Signal Processing*, 2010, pp. 71-76: IEEE.

[52] A. J. Bell and T. J. Sejnowski, "An information-maximization approach to blind separation and blind deconvolution," *Neural computation,* vol. 7, no. 6, pp. 1129-1159, 1995.

[53] T.-W. Lee, M. Girolami, and T. J. Sejnowski, "Independent component analysis using an extended infomax algorithm for mixed subgaussian and supergaussian sources," *Neural computation,* vol. 11, no. 2, pp. 417-441, 1999.

[54] C.-K. Wong, V. Zotev, M. Misaki, R. Phillips, Q. Luo, and J. Bodurka, "Automatic EEG-assisted retrospective motion correction for fMRI (aE-REMCOR)," *Neuroimage,* vol. 129, p. 133, 2016.

[55] V. Zotev, H. Yuan, R. Phillips, and J. Bodurka, "EEG-assisted retrospective motion correction for fMRI: E-REMCOR," *NeuroImage,* vol. 63, no. 2, pp. 698-712, 2012.

[56] L. Pion-Tonachini, K. Kreutz-Delgado, and S. Makeig, "ICLabel: An automated electroencephalographic independent component classifier, dataset, and website," *NeuroImage,* vol. 198, pp. 181-197, 2019.

[57] T. A. Victor *et al.*, "Tulsa 1000: a naturalistic study protocol for multilevel assessment and outcome prediction in a large psychiatric sample," *BMJ open,* vol. 8, no. 1, p. e016620, 2018.

[58] T. Eichele, M. Moosmann, L. Wu, I. Gutberlet, and S. Debener, "Removal of MRI artifacts from EEG recordings," *Simultaneous EEG and fMRI: Recording, Analysis, and Applications,* vol. 2, pp. 95-106, 2010.

[59] S. C. Matthews, A. N. Simmons, E. Arce, and M. P. Paulus, "Dissociation of inhibition from error processing using a parametric inhibitory task during functional magnetic resonance imaging," *Neuroreport,* vol. 16, no. 7, pp. 755-760, 2005.

[60] A. Kok, J. R. Ramautar, M. B. De Ruiter, G. P. Band, and K. R. Ridderinkhof, "ERP components associated with successful and unsuccessful stopping in a stop-signal task," *Psychophysiology,* vol. 41, no. 1, pp. 9-20, 2004.

[61] J. Ramautar, A. Kok, and K. Ridderinkhof, "Effects of stop-signal probability in the stop-signal paradigm: the N2/P3 complex further validated," *Brain and cognition,* vol. 56, no. 2, pp. 234-252, 2004.

[62] J. Ramautar, A. Kok, and K. Ridderinkhof, "Effects of stop-signal modality on the N2/P3 complex elicited in the stop-signal paradigm," *Biological psychology,* vol. 72, no. 1, pp. 96-109, 2006.

[63] L. Carretié, "Exogenous (automatic) attention to emotional stimuli: a review," *Cognitive, Affective, & Behavioral Neuroscience,* vol. 14, no. 4, pp. 1228-1258, 2014.

[64] S. J. Luck and E. S. Kappenman, *The Oxford handbook of event-related potential components*. Oxford university press, 2011.

[65] M. X. Cohen, *Analyzing neural time series data: theory and practice*. MIT press, 2014.

[66] S. J. Luck, *An introduction to the event-related potential technique*. MIT press, 2014.

[67] H. Nolan, R. Whelan, and R. B. Reilly, "FASTER: fully automated statistical thresholding for EEG artifact rejection," *Journal of neuroscience methods,* vol. 192, no. 1, pp. 152-162, 2010.

[68] L. Frølich, T. S. Andersen, and M. Mørup, "Classification of independent components of EEG into multiple artifact classes," *Psychophysiology,* vol. 52, no. 1, pp. 32-45, 2015.

[69] M. Chaumon, D. V. Bishop, and N. A. Busch, "A practical guide to the selection of independent components of the electroencephalogram for artifact correction," *Journal of neuroscience methods,* vol. 250, pp. 47-63, 2015.

[70] A. Mognon, J. Jovicich, L. Bruzzone, and M. Buiatti, "ADJUST: An automatic EEG artifact detector based on the joint use of spatial and temporal features," *Psychophysiology,* vol. 48, no. 2, pp. 229-240, 2011.

[71] I. Winkler, S. Brandl, F. Horn, E. Waldburger, C. Allefeld, and M. Tangermann, "Robust artifactual independent component classification for BCI practitioners," *Journal of neural engineering,* vol. 11, no. 3, p. 035013, 2014.

[72] I. Winkler, S. Haufe, and M. Tangermann, "Automatic classification of artifactual ICA-components for artifact removal in EEG signals," *Behavioral and Brain Functions,* vol. 7, no. 1, p. 30, 2011.

[73] F. C. Viola, J. Thorne, B. Edmonds, T. Schneider, T. Eichele, and S. Debener, "Semi-automatic identification of independent components representing EEG artifact," *Clinical Neurophysiology,* vol. 120, no. 5, pp. 868-877, 2009.

[74] M. D. Fox and M. Greicius, "Clinical applications of resting state functional connectivity," *Frontiers in systems neuroscience,* vol. 4, p. 19, 2010.

[75] K. Smitha *et al.*, "Resting state fMRI: A review on methods in resting state connectivity analysis and resting state networks," *The neuroradiology journal,* vol. 30, no. 4, pp. 305-317, 2017.

[76] M. H. Lee, C. D. Smyser, and J. S. Shimony, "Resting-state fMRI: a review of methods and clinical applications," *American Journal of neuroradiology,* vol. 34, no. 10, pp. 1866-1872, 2013.

[77] R. Patriat *et al.*, "The effect of resting condition on resting-state fMRI reliability and consistency: a comparison between resting with eyes open, closed, and fixated," *Neuroimage,* vol. 78, pp. 463-473, 2013.

[78] H. Yuan, V. Zotev, R. Phillips, and J. Bodurka, "Correlated slow fluctuations in respiration, EEG, and BOLD fMRI," *Neuroimage,* vol. 79, pp. 81-93, 2013.

[79] M. Falahpour, C. Chang, C. W. Wong, and T. T. Liu, "Template-based prediction of vigilance fluctuations in resting-state fMRI," *Neuroimage,* vol. 174, pp. 317-327, 2018.

[80] B. S. Oken, M. C. Salinsky, and S. Elsas, "Vigilance, alertness, or sustained attention: physiological basis and measurement," *Clinical neurophysiology,* vol. 117, no. 9, pp. 1885-1901, 2006.

[81] C. Sander, T. Hensch, D. A. Wittekind, D. Boettger, and U. Hegerl, "Assessment of wakefulness and brain arousal regulation in psychiatric research," *Neuropsychobiology,* vol. 72, no. 3-4, pp. 195-205, 2015.

[82] D. R. Davies and R. Parasuraman, *The psychology of vigilance*. Academic Pr, 1982.

[83] J. J. Foxe, K. P. Morie, P. J. Laud, M. J. Rowson, E. A. De Bruin, and S. P. Kelly, "Assessing the effects of caffeine and theanine on the maintenance of vigilance during a sustained attention task," *Neuropharmacology,* vol. 62, no. 7, pp. 2320-2327, 2012.

[84] K. Mogg, J. McNamara, M. Powys, H. Rawlinson, A. Seiffer, and B. P. Bradley, "Selective attention to threat: A test of two cognitive models of anxiety," *Cognition & Emotion,* vol. 14, no. 3, pp. 375-399, 2000.

[85] M. I. Posner, "Measuring alertness," *Annals of the New York Academy of Sciences,* vol. 1129, no. 1, pp. 193-199, 2008.

[86] M. Schneider, P. Hathway, L. Leuchs, P. G. Sämann, M. Czisch, and V. I. Spoormaker, "Spontaneous pupil dilations during the resting state are associated with activation of the salience network," *NeuroImage,* vol. 139, pp. 189-201, 2016.

[87] C. Chang *et al.*, "Tracking brain arousal fluctuations with fMRI," *Proceedings of the National Academy of Sciences,* vol. 113, no. 16, pp. 4518-4523, 2016.

[88] U. Hegerl *et al.*, "EEG-vigilance differences between patients with borderline personality disorder, patients with obsessive-compulsive disorder and healthy controls," *European Archives of Psychiatry and Clinical Neuroscience,* vol. 258, no. 3, pp. 137-143, 2008.

[89] S. Sadaghiani, R. Scheeringa, K. Lehongre, B. Morillon, A.-L. Giraud, and A. Kleinschmidt, "Intrinsic connectivity networks, alpha oscillations, and tonic alertness: a simultaneous electroencephalography/functional magnetic resonance imaging study," *Journal of Neuroscience,* vol. 30, no. 30, pp. 10243-10250, 2010.

[90] R. B. Berry, R. Brooks, C. E. Gamaldo, S. M. Harding, C. L. Marcus, and B. V. Vaughn, "The AASM manual for the scoring of sleep and associated events," *Rules, Terminology and Technical Specifications, Darien, Illinois, American Academy of Sleep Medicine,* vol. 176, 2012.

[91] S. G. Horovitz *et al.*, "Low frequency BOLD fluctuations during resting wakefulness and light sleep: A simultaneous EEG-fMRI study," *Human brain mapping,* vol. 29, no. 6, pp. 671-682, 2008.

[92] C. W. Wong, V. Olafsson, O. Tal, and T. T. Liu, "The amplitude of the resting-state fMRI global signal is related to EEG vigilance measures," *Neuroimage,* vol. 83, pp. 983-990, 2013.

[93] E. M. Korf, M. Mölle, J. Born, and H. V. V. Ngo, "Blindfolding during wakefulness causes decrease in sleep slow wave activity," *Physiological reports,* vol. 5, no. 7, p. e13239, 2017.

[94] A. Belyavin and N. A. Wright, "Changes in electrical activity of the brain with vigilance," *Electroencephalography and clinical Neurophysiology,* vol. 66, no. 2, pp. 137-144, 1987.

[95] S. Makeig and M. Inlow, "Lapse in alertness: coherence of fluctuations in performance and EEG spectrum," *Electroencephalography and clinical neurophysiology,* vol. 86, no. 1, pp. 23-35, 1993.

[96] R. J. Barry, A. R. Clarke, S. J. Johnstone, C. A. Magee, and J. A. Rushby, "EEG differences between eyes-closed and eyes-open resting conditions," *Clinical Neurophysiology,* vol. 118, no. 12, pp. 2765-2773, 2007.

[97] Q. Zou *et al.*, "Functional connectivity between the thalamus and visual cortex under eyes closed and eyes open conditions: A resting-state fMRI study," *Human brain mapping,* vol. 30, no. 9, pp. 3066-3078, 2009.

[98] Q. Zou, X. Miao, D. Liu, D. J. Wang, Y. Zhuo, and J.-H. Gao, "Reliability comparison of spontaneous brain activities between BOLD and CBF contrasts in eyes-open and eyes-closed resting states," *Neuroimage,* vol. 121, pp. 91-105, 2015.

[99] Q. Zou *et al.*, "Detecting static and dynamic differences between eyes-closed and eyes-open resting states using ASL and BOLD fMRI," *PloS one,* vol. 10, no. 3, p. e0121757, 2015.

[100] P. R. Murphy, R. G. O'connell, M. O'sullivan, I. H. Robertson, and J. H. Balsters, "Pupil diameter covaries with BOLD activity in human locus coeruleus," *Human brain mapping,* vol. 35, no. 8, pp. 4140-4154, 2014.

[101] D. Yellin, A. Berkovich-Ohana, and R. Malach, "Coupling between pupil fluctuations and resting-state fMRI uncovers a slow build-up of antagonistic responses in the human cortex," *NeuroImage,* vol. 106, pp. 414-427, 2015.

[102] O. Lowenstein, R. Feinberg, and I. E. Loewenfeld, "Pupillary movements during acute and chronic fatigue: A new test for the objective evaluation of tiredness," *Investigative Ophthalmology & Visual Science,* vol. 2, no. 2, pp. 138-157, 1963.

[103] J. W. McLaren, J. C. Erie, and R. F. Brubaker, "Computerized analysis of pupillograms in studies of alertness," *Investigative ophthalmology & visual science,* vol. 33, no. 3, pp. 671-676, 1992.

[104] M. S. Gilzenrat, S. Nieuwenhuis, M. Jepma, and J. D. Cohen, "Pupil diameter tracks changes in control state predicted by the adaptive gain theory of locus coeruleus function," *Cognitive, Affective, & Behavioral Neuroscience,* vol. 10, no. 2, pp. 252-269, 2010.

[105] D. B. Henson and T. Emuh, "Monitoring vigilance during perimetry by using pupillography," *Investigative ophthalmology & visual science,* vol. 51, no. 7, pp. 3540-3543, 2010.

[106] K. P. Pruessmann, M. Weiger, M. B. Scheidegger, and P. Boesiger, "SENSE: sensitivity encoding for fast MRI," *Magnetic resonance in medicine,* vol. 42, no. 5, pp. 952-962, 1999.

[107] R. W. Cox, "AFNI: software for analysis and visualization of functional magnetic resonance neuroimages," *Computers and Biomedical research,* vol. 29, no. 3, pp. 162-173, 1996.

[108] G. H. Glover, T. Q. Li, and D. Ress, "Image-based method for retrospective correction of physiological motion effects in fMRI: RETROICOR," *Magnetic*

Resonance in Medicine: An Official Journal of the International Society for Magnetic Resonance in Medicine, vol. 44, no. 1, pp. 162-167, 2000.

[109] R. M. Birn, M. A. Smith, T. B. Jones, and P. A. Bandettini, "The respiration response function: the temporal dynamics of fMRI signal fluctuations related to changes in respiration," *Neuroimage,* vol. 40, no. 2, pp. 644-654, 2008.

[110] B. B. Avants, N. Tustison, and G. Song, "Advanced normalization tools (ANTS)," *Insight j,* vol. 2, pp. 1-35, 2009.

[111] J. M. Toole and G. B. Boylan, "NEURAL: quantitative features for newborn EEG using Matlab," *arXiv preprint arXiv:1704.05694,* 2017.

[112] R. W. Cox, G. Chen, D. R. Glen, R. C. Reynolds, and P. A. Taylor, "FMRI clustering in AFNI: false-positive rates redux," *Brain connectivity,* vol. 7, no. 3, pp. 152-171, 2017.

[113] H. Laufs *et al.*, "Electroencephalographic signatures of attentional and cognitive default modes in spontaneous brain activity fluctuations at rest," *Proceedings of the national academy of sciences,* vol. 100, no. 19, pp. 11053-11058, 2003.

[114] M. D. Fox, A. Z. Snyder, J. L. Vincent, M. Corbetta, D. C. Van Essen, and M. E. Raichle, "The human brain is intrinsically organized into dynamic, anticorrelated functional networks," *Proceedings of the National Academy of Sciences,* vol. 102, no. 27, pp. 9673-9678, 2005.

[115] J. A. De Havas, S. Parimal, C. S. Soon, and M. W. Chee, "Sleep deprivation reduces default mode network connectivity and anti-correlation during rest and task performance," *Neuroimage,* vol. 59, no. 2, pp. 1745-1751, 2012.

Appendix A. Abbreviations

Term	Description
AAS	Average Artifact Subtraction
ACF	Autocorrelation Function
BCG	Ballistocardiogram
BOLD	Blood-oxygen-level-dependent
DMN	Default Mode Network
EEG	Electroencephalography
ERP	Event Related Potential
APPEAR	Automated Pipeline for EEG Artifact Reduction Recorded during fMRI
fMRI	functional Magnetic Resonance Imaging
fNIRS	Functional Near-Infrared Spectroscopy
FOBP	Frontal and Occipital Beta Power
GLM	General Linear Model
HC	Healthy Control subjects
ICA	Independent Component Analysis
MEG	Magnetoencephalography
MR	Magnetic Resonance
MRI	Magnetic Resonance Imaging
OBS	Optimal Basis Sets
PET	Positron Emission Tomography

rsfMRI	Resting state functional Magnetic Resonance Imaging
SNR	Signal to Noise Ratio
TR	Repetition Time